Competitive CO_2/H_2O Adsorption on CALF-20

Tai T. T. Nguyen[a†], Bhubesh Murugappan Balasubramaniam[a], Nicholas Fylstra[b], Racheal P. S. Huynh[b†], George K. H. Shimizu[b], Arvind Rajendran[a*]

a. Department of Chemical and Materials Engineering, University of Alberta, Edmonton, Canada

b. Department of Chemistry, University of Calgary, Calgary, Canada

Abstract

The equilibrium and breakthrough studies of the H_2O adsorption and the competition of CO_2/H_2O on a physisorbent MOF CALF-20, commercialized for CO_2 capture from cement plants, are reported. Volumetric measurements and thermogravimetry were used to measure the water isotherm at various temperatures and relative humidity (RH) values. A Cubic-Langmuir model was used to describe the water isotherms at different temperatures. Both adsorption and desorption dynamic column breakthrough experiments were performed at different RH values to examine different transitions in the isotherm. To quantify the competitive adsorption of CO_2 and H_2O, both thermogravimetric analysis and dynamic column breakthrough techniques were required. A wide range of relative humidity (RH) values was considered, i.e., 10% to 90% RH. CALF-20 showed high CO_2 loadings for RH was smaller than 47%; showing its exceptional capacity to be deployed for CO_2 capture from industrial flue gas. Beyond 70% RH, water was strongly adsorbed, resulting in a significant loss of CO_2 capacity. In the presence of CO_2, CALF-20 showed an unique phenomena where water adsorption was suppressed making it more favourable for practical applications. The modified Langmuir isotherm model was used to describe the competitive CO_2 loading as a function of water loadings and temperatures. A one-dimensional column model simulates the water dynamic column breakthrough and competitive CO_2/H_2O breakthroughs. Both concentration profiles and temperature histories agreed with the experimental results.

* Corresponding Author : arvind.rajendran@ualberta.ca (A. Rajendran)

† Current Address: Svante Structured Adsorbents Centre of Excellence, Svante Inc. 3021 Underhill Ave., Burnaby, BC V5A 3C2, Canada

1. Introduction

Flue gas from fossil fuel-fired power plants usually contains water vapour along with CO_2, N_2, and O_2. Water has a strong affinity to most solid adsorbents (Xiao et al. 2008, Li et al. 2009, Wilkins et al. 2020), which makes it more difficult to separate CO_2 in the flue gas. Zeolite 13X, a benchmark adsorbent, is a potential candidate for CO_2 capture due to its high CO_2 saturation loading and high CO_2/N_2 selectivity (Rajagopalan et al. 2016). This adsorbent could meet 95% purity and 90% recovery with a dry gas stream, albeit at low vacuum pressures (Rajagopalan et al. 2016). However, the CO_2 capacity of zeolite 13X significantly decreases in the presence of even trace amounts of water (≈1% relative humidity (RH)) (Hefti et al. 2018, Wilkins et al. 2020). Metal-organic frameworks (MOFs), a relatively new class of hybrid porous materials, have seen significant advances in the recent past (Yu et al. 2017, Altintas et al. 2018). The structure of MOFs is porous, predictable, tunable, and highly crystalline (Yaghi et al. 1999). Their structures can be designed and modified to be deployed in a specific application. MOFs for CO_2 capture, especially water-stable MOFs, are desirable for capturing CO_2 in moist conditions without losing their performance (Chanut et al. 2017).

A water-stable MOF should preserve its structure after exposure to water. This alone would not translate to the capture of CO_2 in wet gas, but it is a requisite first step. To meet this expectation, MOFs should be constructed from highly coordinated metal nodes and/or have strong metal-linker bonds to protect the coordination sites (Burtch et al. 2014, Canivet et al. 2014, Chanut et al. 2017). Several computational and experimental studies have been reported to develop new MOFs for CO_2 capture with high water stability (Sumida et al. 2012, Burtch et al. 2014). Studying the adsorption equilibrium of water is necessary to design and synthesize sorbents for practical applications. Depending on the surface properties, the adsorbent could exhibit a rectangular type I isotherm, which shows a very strong affinity to water and reaches the saturation capacity at a very small relative humidity (Wilkins et al. 2020). High temperatures and/or low vacuum are required to desorb water, making it challenging (Wilkins et al. 2020). It is common to observe Type V isotherms, particularly on hydrophobic surfaces, e.g., activated carbons (Hefti et al. 2015). Activated carbons show unfavourable water adsorption at low relative humidity and become a favourable isotherm at high relative humidity (Hefti et al. 2015). However, the adsorbent is not suitable for CO_2 capture owing to its low CO_2/N_2 selectivity. Often, water isotherms show a hysteresis loop with inflection points (Velasco et al. 2016). The water loading in the desorption

curve is higher than the adsorption one at the same relative humidity, usually caused by capillary condensation (Thommes et al. 2006, Velasco et al. 2016). Owing to the shape and the presence of hysteresis of the isotherm, complicated models are required to describe the equilibrium relationship (Zhang et al. 2006, Hefti et al. 2015, Pai et al. 2019).

Measuring the water equilibrium loading is challenging and possibly time-consuming, unlike non-condensable gases. Key challenges are related to the reliability of detectors, i.e., RH meters, stable water vapour generation, and vapour condensation (Hefti et al. 2015). Most studies dealing with CO_2 capture typically ignore water, making an implicit assumption that water is removed in an upstream operation. Furthermore, water breakthrough studies are also required for better insights into the column dynamics. Only a few studies on water breakthroughs have been reported, particularly in the context of sorbents for CO2 capture. Hefti and co-workers studied the adsorption and desorption breakthrough of water vapour on activated carbon at 45°C with different feed velocities (Hefti et al. 2015). Both adsorption and desorption breakthrough curves showed many transitions due to an inflection point in the isotherm (Hefti et al. 2015). Wilkins *et al*. reported the adsorption breakthrough of water on zeolite 13X at different relative humidities (Wilkins et al. 2020). A sharp front was observed in all breakthrough curves due to the rectangular type I isotherm (Wilkins et al. 2020). Goyal and co-workers studied the water adsorption and desorption on silica gel at different RH values (Goyal et al. 2020). While the adsorption breakthrough curve at 83% RH showed a sharp front, the desorption curve of silica gel at the same RH showed a shock and a wave due to a hysteresis loop from 25% to 85% RH (Goyal et al. 2020). Silva et al. performed the water adsorption and desorption breakthrough on MIL-160(Al) at 50% RH and 25°C (Silva et al. 2021). A simple wave and a shock transition were observed in the adsorption breakthrough curve, indicating the presence of an inflection point in the water isotherm. Similarly, the MIL-160(Al) desorption curve showed a shock followed by a wave, confirming the existence of an inflection point (Silva et al. 2021).

A practical adsorbent for CO_2 capture requires that water does not adversely impact CO_2 adsorption and is structurally stable in the presence of water (Rajendran et al., 2023). While deployment in a wet gas stream is typical for chemisorbents, albeit at the cost of higher regeneration energies, it can be a crucial factor for a CO_2 physisorbent, as water typically outcompetes CO_2. The benchmark adsorbent, Zeolite 13X, shows poor performance in the

presence of water (Wilkins et al. 2020). A decrease of ≈90% in the competitive CO_2 loading is seen in zeolite 13X at 5% relative humidity (RH) (Wilkins et al. 2020). Furthermore, removing water from zeolite 13X is extremely difficult since it exhibits a rectangular type I isotherm with a high saturation capacity at ≈17 mmol/g (Hefti et al. 2015, Wilkins et al. 2020). Mg-MOF-74 is a potential candidate for CO_2 capture due to its high CO_2 capacity, up to 7.0 mmol/g at 0.15 bar partial pressure (Bahamon et al. 2018, Ben-Mansour et al. 2018, Qasem et al. 2018). However, the water isotherm on Mg-MOF-74 also exhibits a type I isotherm with a saturation capacity of ≈35 mmol/g (Qasem et al. 2018). Thus, a significant decrease in CO_2 loading was also observed under wet conditions (Kizzie et al. 2011, Chanut et al. 2017). Further, Mg-MOF-64 is unstable in the presence of water (DeCoste et al., 2013). Amine-based adsorbents are also highly attractive due to their high CO_2 capacities and diverse subclasses (Gelles et al. 2020, Varghese et al. 2020), e.g. mesoporous silica MCM-41 triamine-grafted (Belmabkhout et al. 2010), polyethylenimine (PEI) modified porous silica (Choi et al. 2011), amine-based nano-fibrillated cellulose (Gebald et al. 2011), amine-functionalized MIL-101 (Darunte, 2016), etc. The H_2O isotherm of the amine-functionalized cellulose exhibited a type III (unfavourable) isotherm (Gebald et al. 2014). Furthermore, an increase in the CO_2 capacity was observed for this adsorbent under moist conditions (Gebald et al. 2014, Stampi-Bombelli et al. 2020).

Understanding the competition between CO_2 and H_2O is crucial to designing an adsorption process for CO_2 capture. Several studies on the effect of water on CO_2 were reported. Levan's group examined the reduction of CO_2 loading on HKUST-1 under different RH values using a volumetric system coupled with gas chromatography (GC). HKUST-1 showed a type II isotherm with two inflection points, and the saturation capacity of water was ≈40 mmol/g (Liu. et al. 2010). The competitive water loading on HKUST-1 was not affected by the adsorption of CO_2. However, the CO_2 capacity dropped in the presence of water, nearly zero at the relative humidity of 67% RH (Liu. et al. 2010). The decrease of CO_2 loading in wet conditions on HKUST-1 and MIL-101(Cr) was also confirmed by Pirngruber *et al*. (Pirngruber et al. 2012). The effect of water on CO_2 loading was also studied on MIL-101(Cr) using the dynamic column breakthrough technique. The column was saturated with water vapour initially, then CO_2 was introduced into the column. A zero loading of CO_2 was observed from this study, indicating that water was strongly adsorbed (Pirngruber et al. 2012).

In this study, the adsorption of H_2O and the competitive adsorption of CO_2/H_2O on CALF-20 are reported. CALF-20 is a MOF containing Zinc ions connected by 1,2,4-triazolate and oxalate linkers. Specifically, it has a formula [Zn_2(1,2,4-triazolate)$_2$(oxalate)]. Moreover, CALF-20 is one of the first MOFs to be scaled up for CO_2 capture from industrial flue gas and has garnered significant attention (Lin et al. 2021, Nguyen, 2021). Water isotherms on CALF-20 were measured from 22°C to 100°C at various RH values using volumetric and thermogravimetric techniques. A Cubic-Langmuir isotherm model described the water adsorption and desorption equilibrium. Both adsorption and desorption dynamic column breakthrough (DCB) experiments were performed at 22°C and various RH values. A combination of thermogravimetric analyzer (TGA) and binary dynamic column breakthrough (DCB) experiments were performed at various relative humidity values to quantify the equilibrium loading of each component in the binary adsorption. A one-dimensional column model including heat transfer, mass transfer, dispersion and pressure drop was used to simulate the H_2O breakthroughs and the competitive CO_2+H_2O DCB at various RH values. A modified Langmuir isotherm described the competitive CO_2 isotherm, while the cubic Langmuir isotherm model described the competitive water isotherm. All breakthrough curve temperature histories from the experiments and simulations are reported. It is worth pointing out that the pure water adsorption data and the raw breakthrough data for CO_2+H_2O competitive experiments were reported in our previous work (Lin et al. 2021). They are reported here for completeness. In addition to presenting these results, important new insights not described earlier are highlighted here. The modelling of the isotherms (H_2O and CO_2+H_2O), pure water breakthrough experiments and the modelling of all pure water and CO_2+H_2O competitive breakthrough experiments are reported in this work for the first time. Results of stability tests are also present to highlight the excellent robustness of CALF-20 towards moisture.

2. Materials and methods

2.1. Materials

CALF-20 was synthesized and characterized at the University of Calgary. Powdered CALF-20 was structured by the phase inversion method mentioned in the previous study (Lin et al. 2021). The powdered CALF-20 was formed into cylindrical extrudates of 1mm diameter and 1-3 mm length by adding 20 wt% polysulfone. The particle density of the structured CALF-20 was estimated at 570 kg/m^3. Instrument air was the carrier gas to create a humid stream for single-

component H_2O dynamic column breakthrough studies. CO_2 was used as a carrier gas for binary dynamic column breakthrough experiments. Pure Helium (99.998%) and pure CO_2 (99.998%) were purchased from Praxair Canada Inc. The humidifier containing deionized water was used in all experiments to create humid gas.

2.2. Static measurements

The determination of the adsorption behaviour of water on the adsorbent is critical for process design. Most practical applications of CO_2 capture involve flue gas that is fully (or partially) saturated with water as it is a combustion product. Despite this, a literature scan reveals that few studies consider water adsorption. Part of this observation can be attributed to the challenges of performing water vapour experiments (Hefti et al. 2015). Extreme care must ensure water does not condense anywhere within the experimental setup. Further, the measurement of RH is important. These aspects were carefully considered in this study. Single-component water isotherms were measured by volumetric and thermogravimetric analysis (TGA). These were finally compared to values obtained from dynamic column breakthrough (DCB) experiments

Volumetric measurements

Water isotherms at 22°C were measured by the Micromeritics ASAP 2020 (Norcross, GA, USA) available at the University of Calgary. The ASAP 2020, equipped with an enhanced water vapour generation unit, allows measuring the H_2O adsorption equilibrium at very low RH. Both adsorption and desorption isotherms were measured at 22°C from 0% RH to ≈ 100% RH. A mass of ≈200 mg structured CALF-20 was used for these measurements. Before the measurement, the adsorbents were activated at 150°C for 12 hours. At first, the sample cell containing the adsorbent was evacuated. The volumetric equilibrium data was collected by dosing a known amount of gas into the sample cell. The adsorbed amount was calculated by monitoring the pressure change and solving the mass balance. The accuracy of this system is 0.15% of reading, and the pressure accuracy is 1.3×10^{-7} mbar.

Thermogravimetric analysis

A TA Q500 Thermogravimetric Analyzer (TGA) obtained from TA Instruments, DE, USA was used to measure single component H_2O isotherms and the total CO_2+H_2O loadings at ≈0.97 bar total pressure, several temperatures and various RH values. As shown in Fig. 1, a custom-made bubbler humidifier generated a stable humid stream at the desired RH level. This humidifier

contains a tank filled with deionized water. Two mass flow controllers, MFC-1 and MFC-2 (Alicat Scientific, Tucson, AZ, USA), were used to achieve the desired value of RH. Dry gas was divided into two separate streams to generate a humid gas stream. The first stream passed through MFC-2 and was introduced at the bottom of the tank. After bubbling through the tank, this stream, saturated with water, was mixed with the second dry stream (passed through the MFC-1). The relative humidity of this mixed stream was measured by the RH1 (SensorPush, Brooklyn, NY, USA) to ensure that the desired RH value was reached. It is worth noting that in the design available in our laboratory, it took approximately 5-6 hours for the RH value to stabilize. Note that the RH can be controlled by adjusting the flow rates in MFC-1 and MFC-2 suitably. The humid stream was then introduced to the TGA chamber containing ≈65 mg of the structured CALF-20 at the desired temperature. The total mass of the sample was measured and recorded over time. The equilibrium is reached when the mass change of the sample is less than 0.01%. For the experiments related to pure water uptake, the difference between the initial and final mass of the sample is the amount of H_2O adsorbed. The equilibrium loadings were measured at various RH values and temperatures, namely, 22, 30, 40, 50, 60, 80 and 100°C. For pure H_2O adsorption measurements, dry instrument air was used as a carrier gas. The constituents of the instrument air (N_2, O_2 and Ar) were assumed to have negligible affinity in the presence of water. In the case of competitive CO_2+H_2O adsorption, only the total amount, i.e., the sum of CO_2 and H_2O adsorbed can be measured. Before the experiment, the adsorbent was activated by purging with air at atmospheric pressure and 150°C for 12 hours. The weighing precision of this TGA is ±0.01%, and the sensitivity is 0.1µg.

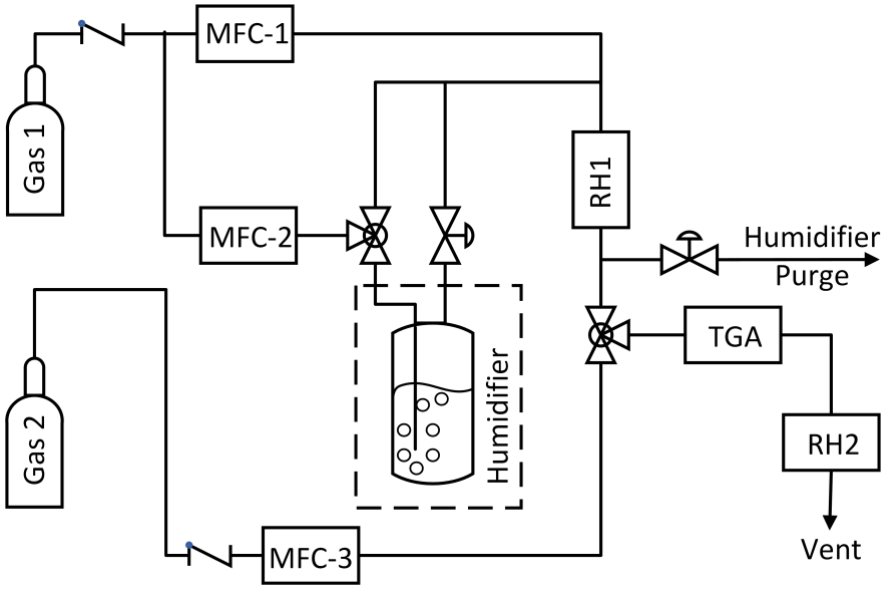

Figure 1: The schematic of the modified thermogravimetric analyzer coupled with the bubble humidifier for measuring water isotherms and the total CO_2+H_2O adsorption; MFC – Mass flow controller, RH - Relative humidity meter; TGA – Thermogravimetric analyzer

2.3. Dynamic column breakthrough studies

The dynamic column breakthrough (DCB) apparatus reported in our previous study was used to perform water DCB experiments and the binary CO_2/H_2O breakthrough studies (Nguyen et al. 2022). A bubbler humidifier was added to this DCB setup, as shown in Fig. 2, to create a humid stream. A 40 mL stainless steel column (Swagelok 304L-HDF2-40, length 7.86 cm; inner diameter 2.82 cm) packed with 16.7 g structured CALF-20 was used. Two relative humidity meters (SensorPush, Brooklyn, NY, USA) were placed at the inlet and outlet of the column, respectively, to measure the relative humidity. The temperature accuracy of this SensorPush is ±0.3°C, and the humidity accuracy is ±3%. A pressure transducer and a differential pressure gauge (GE Druck, Billerica, MA, USA) measured the inlet pressure and pressure drop across the column. The column thermal history was measured by a thermocouple (Omega Engineering, Laval, QC, Canada) placed 1.82 cm from the outlet. A mass spectrometer (Pfeiffer Vacuum OmniStar GSD 320, Asslar, Germany) was placed at the outlet to record the composition of the effluent gas. All data were recorded every second automatically by a Labview data acquisition system. Before the start of any experiment, sufficient time was provided to create a steady, humid stream. The column was activated at 150°C for 12 hours using helium as a purge gas.

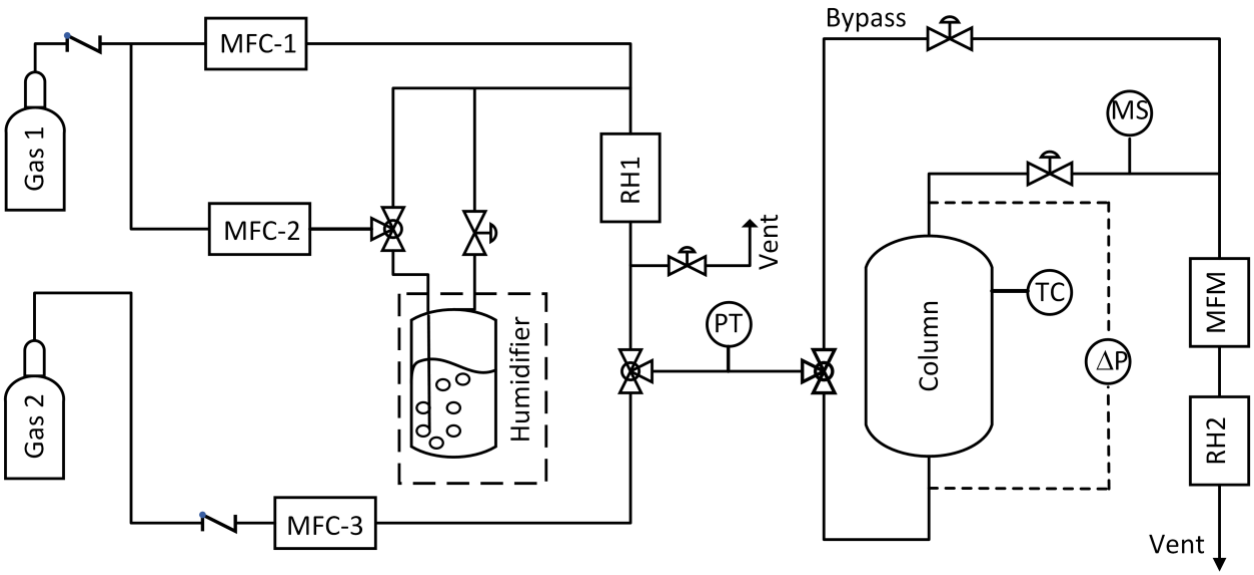

Figure 2: Schematic diagram of the dynamic column breakthrough apparatus with the humidifier. MFC - Mass flow controller; RH - Relative humidity meter; PT - Pressure transducer; TC - Thermocouple; MS - Mass spectrometer; MFM - Mass flow meter

In adsorption experiments, the column was first saturated with an inert gas (Helium). At $t = 0$, the humid stream was fed to the column. The column temperature history, the gas composition and the outlet RH were recorded over time. A data acquisition system also recorded the inlet and outlet flow and the pressure history. The adsorption experiment is completed when the outlet composition and temperature equalled the inlet. In the single-component H_2O breakthrough experiments, three H_2O adsorption experiments were performed: 8%, 22% and 45% RH. For binary CO_2/H_2O breakthrough, a range of RH values, i.e., 13%, 18%, 23%, 32%, 45%, 70% and 88% RH, were chosen for individual DCB experiments. All breakthrough experiments were run at ≈22°C and 0.97 bar total pressure. Before each experiment, the column was regenerated at 150°C for 12 hours. The humidifier was set to run until a stable desired RH value was obtained before the experiment.

In the single-component H_2O desorption experiments, the bed was initially equilibrated at a certain RH level (8%, 22% or 45% RH). At $t = 0$, dry instrument air was introduced to the column. The column temperature and the outlet RH were measured. The desorption experiment is completed when the outlet RH is nearly 0% (within sensor accuracy) and the temperature equals the surrounding environment.

Before the experiments, all mass flow controllers and mass flow meters were calibrated by a universal gas flow meter (Agilent Technologies, Santa Clara, CA, USA). The blank response was also performed, and it was negligible. This is reasonable since the blank response was less than 5 seconds, and the entire adsorption/desorption experiments took longer than two days.

2.4. Difficulties in performing water breakthrough experiments

Before performing a humid breakthrough experiment, many uncertainties need to be addressed. First, water condensation in the system might happen at the saturation condition (Hefti et al. 2015). Once this phenomenon occurs, it is difficult to completely remove condensed water from the column. The humid breakthrough experiments were operated far from the dew point to avoid water condensation. Furthermore, to create a stable humid stream, the bubbler humidifier must run at a constant flow rate for a long time (≈6 hours). Note that the tank's water volume was ≈250 mL and the total flow rate was ≈200 ccm. This ensures the steady state was reached and a constant relative humidity feed was generated and maintained (Wilkins et al. 2020). Measuring the relative humidity was also challenging since it depended on temperature and pressure. Under the presence of CO_2, more challenges need to be mentioned. CO_2 can dissolve in water, so it requires longer to generate a constant humid stream. CO2 influences the signal of many RH sensors (Lorek et al. 2018, Wilkins et al. 2020). To examine the effect of CO_2 on the RH signal, a humid gas was generated at a fixed ratio of dry and wet flowrates using two different carrier gases. In the first experiment, instrument air was used as a carrier gas, and in the following experiment, the carrier gas was replaced with CO_2. A similar relative humidity signal should be obtained in these two experiments since the pressure and temperature of the system were kept identical, and the equipment was operated at low pressures. However, a lower relative humidity value was observed under CO_2. To correct the RH signal in the CO_2 environment, a calibration curve was built by performing similar experiments using instrument air and pure CO_2 as carrier gases. The calibration was performed at 22°C and 0.97 bar total pressure provided the following relationship:

$$RH_{CO_2}^{\text{corrected}} = 1.2583 RH_{CO_2}^{\text{measured}} - 2.4031 \quad (1)$$

This RH calibration curve is only valid within the scope of the experimental conditions in this study. A suitable RH calibration would need to be constructed if experiments were performed at different conditions.

3. Column modelling and simulations

3.1.Detailed column model for dynamic column breakthrough simulations

A one-dimensional mathematical model including dispersion, convection, heat transfer and pressure drop, was applied to simulate the column dynamics. The following assumptions were made in this model:

- The gas phase is ideal
- There is no composition and temperature gradient in the radial direction, i.e., the column is one-dimensional.
- Axial dispersion is included
- Darcy's law is used to describe the pressure drop
- The ambient temperature is stable
- Local thermal equilibrium between the gas and the solid phase is established instantaneously
- The adsorbent's properties are uniform along the column
- The linear driving force (LDF) is adequate to describe the mass transfer in the solid phase

A set of partial differential equations (PDE) and boundary conditions were discretized by using the finite volume method. The column was split into 30 cells, and the obtaining set of ordinary differential equations (ODE) was solved by a MATLAB ODE solver (*ode23s*). All equations in this model were reported in our previous studies (Nguyen et al. 2022, Nguyen et al. 2022) and are summarized in Table 1.

Table 1: A summary of equations for the detailed column model

Component mass balance	$\frac{\partial y_i}{\partial t} + \frac{y_i}{P}\frac{\partial P}{\partial t} - \frac{y_i}{T}\frac{\partial T}{\partial t} = D_L \frac{T}{P}\frac{\partial}{\partial z}\left(\frac{P}{T}\frac{\partial y_i}{\partial z}\right) - \frac{T}{P}\frac{\partial}{\partial z}\left(\frac{P y_i}{T} v\right) - \frac{RT}{P}\frac{1-\varepsilon}{\varepsilon}\frac{\partial q_i}{\partial t}$
Total mass balance	$\frac{1}{P}\frac{\partial P}{\partial t} - \frac{1}{T}\frac{\partial T}{\partial t} = -\frac{T}{P}\frac{\partial}{\partial z}\left(\frac{P}{T} v\right) - \frac{RT}{P}\frac{1-\varepsilon}{\varepsilon}\sum_{i=1}^{n_{comp}}\frac{\partial q_i}{\partial t}$
Solid phase mass balance	$\frac{\partial q_i}{\partial t} = k_i(q_i^* - q_i)$
Pressure drop	$-\frac{\partial P}{\partial z} = \frac{150}{4}\frac{1}{r_p^2}\left(\frac{1-\varepsilon}{\varepsilon}\right)^2 \mu v$

Column energy balance	$\left[\frac{1-\varepsilon}{\varepsilon}\left(\rho_s C_{p,s} + C_{p,a}\sum_{i=1}^{n_{comp}} q_i\right)\right]\frac{\partial T}{\partial t} = \frac{K_z}{\varepsilon}\frac{\partial^2 t}{\partial z^2} - \frac{C_{p,g}}{R}\frac{\partial}{\partial z}(vP) - \frac{C_{p,g}}{R}\frac{\partial P}{\partial t} - \frac{1-\varepsilon}{\varepsilon}C_{p,a}T\sum_{i=1}^{n_{comp}}\frac{\partial q_i}{\partial t} + \frac{1-\varepsilon}{\varepsilon}\sum_{i=1}^{n_{comp}}\left((-\Delta H_i)\frac{\partial q_i}{\partial t}\right) - \frac{2h_{in}}{\varepsilon r_{in}}(T - T_w)$
Wall energy balance	$\rho_w C_{p,w}\frac{\partial T_w}{\partial t} = K_w\frac{\partial^2 T_w}{\partial z^2} + \frac{2r_{in}h_{in}}{r_{out}^2 - r_{in}^2}(T - T_w) - \frac{2r_{out}h_{out}}{r_{out}^2 - r_{in}^2}(T_w - T_{amb})$

3.2. Mass balance calculations

A mass balance around the column is written for each dynamic column breakthrough experiment to calculate the H_2O loading in the solid phase at equilibrium. Since no reaction occurs, the mass balance can be written as

$$n_{in} - n_{out} = n_{acc} \tag{2}$$

where n_{in} and n_{out} are the total number of moles at the inlet and outlet respectively, n_{acc} is the accumulation in the fluid and solid phases. When ideal gas law is assumed, this mass balance equation can be written as:

$$\int_0^\infty \left(\frac{Q_{in}P_{avg}y_{i,in}}{RT_{in}}\right)dt - \int_0^\infty \left(\frac{Q_{out}P_{avg}y_{i,out}}{RT_{out}}\right)dt = q_i^* m_{ads} + \frac{P_{avg}y_{i,in}}{RT_{in}}V_b\varepsilon + \frac{P_{avg}y_{i,in}}{RT_{in}}V_d \tag{3}$$

where Q_{in} and Q_{out} are the inlet and outlet flow rates, respectively, y_i is the composition of component *i* in the fluid phase, *P* and *T* denote the total pressure and the temperature, m_{ads} is the total weight of the adsorbent, V_b and V_d are the column volume and the total dead volume of the system, respectively. Solving Eqn. (3) will provide the solid equilibrium loading of component *i*, *i.e.*, q_i^* . Assuming the column pressure drop is negligible, the average pressure of the

column$\left(P_{avg} = \frac{P_{in}+P_{out}}{2}\right)$ can be used in this equation. To obtain a reliable solid loading q_i^*, a complete adsorption breakthrough is required where the concentration front and the thermal waves have been broken through the column.

To estimate the competitive CO_2 loadings, the Eqn. (3) can be used. Another expression can be written to reflect the competitive CO_2 loading (Wilkins et al., 2019):

$$\int_0^{t_{ads}} \left[1 - \frac{Q_{out}y_{i,out}}{Q_{in}y_{i,in}}\right] dt = \frac{RT}{Q_{in}P_{avg}y_{i,in}} \left[q_i^* m_{ads} + C_{avg}V_b\varepsilon + C_{avg}V_d\right] \quad (4)$$

$$C_{avg} = \frac{P_{avg}y_{i,in}}{RT} \quad (5)$$

Note that in the system where one component is more strongly adsorbed than the other, the expression on the left-hand side of the Eqn. (4) might result in a negative value if the accuracies of the composition and flow measurements are not high (Wilkins et al., 2019). The literature proposes desorption experiments starting from a column saturated with a mixture (Wilkins et al. 2019). This study proposes a different approach that employs two independent techniques, namely TGA and DCB, to estimate the competitive loading of CO_2. We adopt this approach, particularly considering the long breakthrough times for H_2O that can cause substantial challenges in evaluating the CO_2 loadings.

In the pure water desorption breakthroughs, the water loadings can be estimated by performing the following mass balance:

$$n_{out} = n_{acc} \quad (6)$$

$$q_i^* = \frac{1}{m_{ads}} \left[\int_0^{\infty} \left(\frac{Q_{out}P_{avg}y_{i,out}}{RT_{out}}\right) dt\right] \quad (7)$$

4. Results and Discussions

4.1. Single component water isotherms

Pure water isotherms were measured at various temperatures (22, 30, 40, 50, 60, 80 and 100°C), from 0 bar to 0.027 bar partial pressure by TA Q500 thermogravimetric analyzer. All H_2O equilibrium data are shown in Fig. 3. An S-shape isotherm with an inflection point (Type V) was

observed (Sing et al. 1985, Thommes et al. 2015). The characteristic S-shape is clearly seen at lower temperatures (22°C and 30°C). The H_2O loadings on CALF-20 strongly depend on the temperature. Only a very small amount of H_2O (< 0.5 mmol/g) was adsorbed at over 80°C within the experimental pressure range. Furthermore, at a low partial pressure of H_2O (<10% RH, at 22°C), CALF-20 showed little to no adsorbed amount of H_2O.

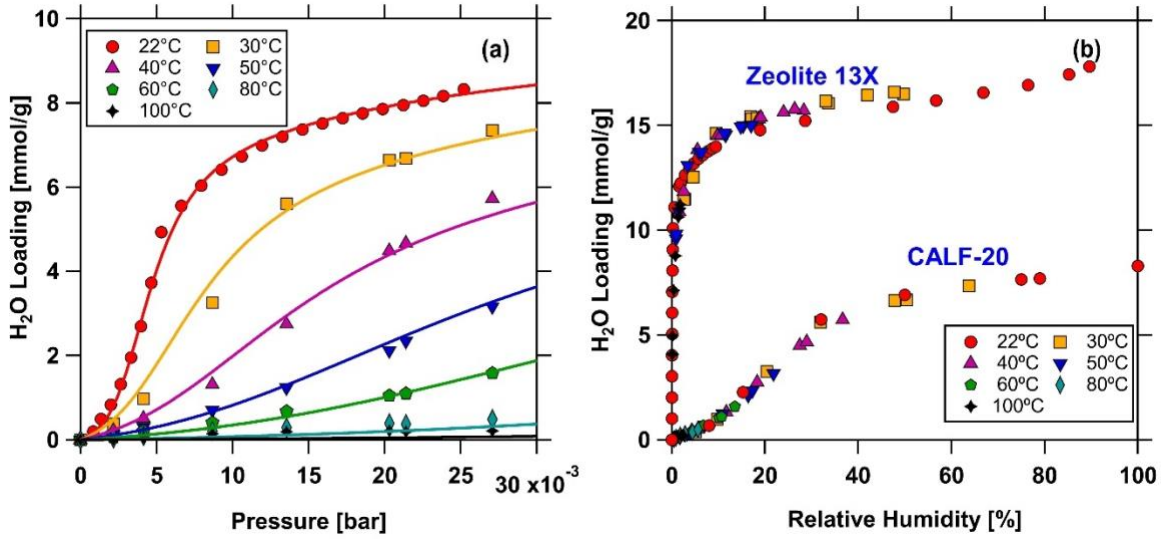

Figure 3: H_2O adsorption isotherms on structured CALF-20. (a) Water isotherms of CALF-20 as a function of pressure at various temperatures. (b) Comparison of H_2O isotherms on CALF-20 and zeolite 13X at different temperatures as a function of RH. Markers represent the experimental data, and solid lines are the fitted isotherms. Zeolite 13X data were obtained from Wilkins and Rajendran (Wilkins et al. 2020).

Figure 3b shows the same data as in Fig. 3a but is now plotted as a function of RH. Like many materials, when the loadings are plotted as a function of RH, the isotherms at various temperatures collapse onto one another. The corresponding water loading on the current benchmark CO_2 capture material (zeolite 13X) is plotted alongside (Wilkins et al. 2020). A few important observations can be made. First, the saturation capacity of water on CALF-20 is much lower compared to zeolite 13X. Second, while the water isotherm on zeolite 13X resembles a type I isotherm, that on CALF-20 follows a type V isotherm. Finally, it is also noticeable that the water loading of CALF-20 up to ≈ 10% RH is very small. Under corresponding conditions, H_2O loading on zeolite 13X is almost close to saturation. These observations indicate that CALF-20 will be attractive for practical

applications. Recently, Chen et al. have shown that CALF-20 undergoes a polymorphic transformation induced by exposure to humidty (Chen et al., 2023). Particularly they show that the transformation occurs around 11-23% RH, i.e.,, is the same region where the infelction point in the H_2O isotherm has been seen.

The isosteric heat of adsorption for water on CALF-20 shown in Fig. 4 was calculated by the Clausius-Clapeyron equation using the isotherm data at different temperatures:

$$\left(\frac{\partial \ln p_i}{\partial(1/T)}\right)_{q_i} = -\frac{\Delta H_{iso}}{R} \tag{8}$$

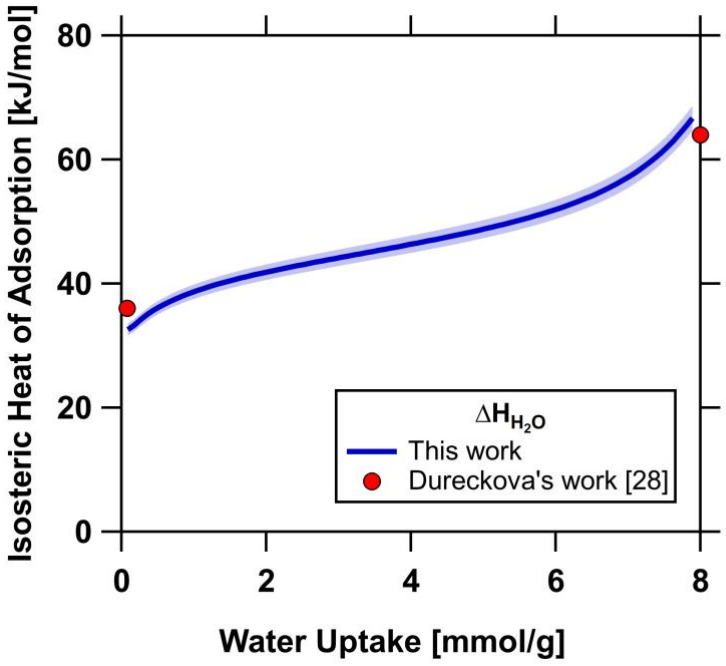

Figure 4: Isosteric heat of adsorption for H_2O on CALF-20 calculated from three different temperatures (22°C, 30°C and 40°C) using the Clausius-Clapeyron equation. The solid line is the isosteric heat of adsorption for H_2O on CALF-20 calculated from fitted isotherms in this work. The shading area indicates 3% of uncertainty in the fitting data. The circle markers are the data collected from molecular simulation from Dureckova's work (Dureckova 2018).

Figure 4 shows the variation of isosteric heat of water adsorption on CALF-20. The isosteric heat was calculated from the fitted isotherm data at 22°C, 30°C and 40°C using the Cubic -Langmuir model that will be introduced later. At lower H_2O loadings, the H_2O heat of adsorption is ≈35

kJ/mol, which implies a low affinity of H_2O onto the adsorbent. We note that the heat of water adsorption at low loadings is lower than that of CO_2 ≈39 kJ/mol, contributing to favourable CO2 adsorption at low humidities. When the H_2O loading increases, the isosteric heat of adsorption of H_2O also increases, implying strong sorbate-sorbate interactions. A slight discrepancy between the fitted isotherms and the experimental data was observed during the fitting procedure. Thus, a 3% uncertainty was estimated based on the calculation of the isosteric heat of adsorption. The magnitude of the isosteric heat of adsorption for water on CALF-20 is comparable with the molecular simulations reported by Dureckova (Dureckova 2018). The isosteric heat of adsorption on CALF-20 at 1% RH and 100% RH were predicted to be 36 kJ/mol and 64 kJ/mol, respectively (Dureckova 2018).

4.3. Descriptions of water adsorption isotherms

Describing isotherms with inflection points is challenging (Martinez et al. 1996, Ilić et al. 2010, Hefti et al. 2015, Pai et al. 2019). An inflection point on the isotherm can be caused by different reasons such as multi-layer adsorption, phase transitions, capillary condensation phenomenon, and change in the sorbent structure (Thommes et al. 2006, Thommes 2010). Based on an early work on the lattice statistics by Hill (Hill 1960), and using an m^{th} order Padé approximant (Baker et al. 1996), a general form to describe an adsorption phenomenon can be defined:

$$q_i^*(C_i) = q_{sat,i} C_i \frac{\left[\frac{dv_i(C_i)}{dC_i}\right]}{v_i(C_i)} \tag{9}$$

$$v_i(C_i) = 1 + \sum_j^m b_{i,j}(C_i)^j \tag{10}$$

Where q_i^* and $q_{sat,i}$ denote the equilibrium and saturation loading of component *i*, *C* is the concentration, *b* is the adsorption equilibrium constant. When m is equal to three, a third-order approximation can be obtained:

$$v_i(C_i) = 1 + b_{i,1}C_i + b_{i,2}(C_i)^2 + b_{i,3}(C_i)^3 \tag{11}$$

Replacing the Eqn. (11) into the Eqn. (9), a well-known cubic isotherm model can be written (Ruthven 1984):

$$q_i^*(C_i) = q_{sat,i}\frac{[b_{i,1}C_i + 2b_{i,2}(C_i)^2 + 3b_{i,3}(C_i)^3]}{[1 + b_{i,1}C_i + b_{i,2}(C_i)^2 + b_{i,3}(C_i)^3]} \quad (12)$$

We assume that there are two main adsorption sites for water. The first site is described by a third-order Padé approximation, and the second site is written by a first-order Padé approximation. The resulting model is the so-called Cubic -Langmuir model (Zhang et al. 2006):

$$q_{H_2O}^*(C_{H_2O}) = q_{sb}\frac{[b_1C_{H_2O} + 2b_2(C_{H_2O})^2 + 3b_3(C_{H_2O})^3]}{[1 + b_1C_{H_2O} + b_2(C_{H_2O})^2 + b_3(C_{H_2O})^3]} + q_{sd}\frac{dC_{H_2O}}{1 + dC_{H_2O}} \quad (13)$$

where q_{sb} and q_{sd} represent the saturated loadings of *b* site and *d* site, b_1, b_2 and b_3 are the adsorption equilibrium constants of *b* site, and *d* is the adsorption equilibrium constant of *d* site. To describe the temperature dependence, the Van't Hoff type equation is applied to express the adsorption equilibrium constants following:

$$b_1 = b_{0,1}e^{-\Delta U_1/(RT)} \quad (14)$$

$$b_2 = b_{0,2}e^{-\Delta U_1/(RT)} \quad (15)$$

$$b_3 = b_{0,3}e^{-\Delta U_1/(RT)} \quad (16)$$

$$d = d_0e^{-\Delta U_2/(RT)} \quad (17)$$

where ΔU_1 and ΔU_2 are the internal energy of site *b* and *d*, respectively. Using the H_2O equilibrium experimental isotherms at various temperatures and from 0 bar to 0.027 bar partial pressure, these parameters (q_{sb}, q_{sd}, $b_{0,1}$, $b_{0,2}$, $b_{0,3}$, d_0, ΔU_1 and ΔU_2) can be found. A curve fitting tool in MATLAB (*fmincon*) was used to regress the parameters by fitting the model to the experimental by minimizing the objective function *J*:

$$J = \sum_{i=T_1}^{T_n}\sum_{j=P_1}^{P_m}\left(q^*_{\text{measured}}(T_i, P_{i,j}) - q^*_{\text{fitted}}(T_i, P_{i,j})\right)^2 \quad (18)$$

where the pressure changed from 0 to 0.027 bar, and the temperature varied from 22°C to 100°C. All fitted parameters from the cubic -Langmuir model is given in Table 2. The fitting of the water isotherm parameters as a function of RH is given in Section S1 of the supporting information. Fig. 3a shows a good agreement between the fitted and experimental isotherms at various temperatures. The inflection points on the isotherm at different temperatures are also well captured by this model.

Table 2: Fitted cubic -Langmuir isotherm parameters for pure H_2O on CALF-20

Parameter		Adsorption	Desorption
q_{sb}	mmol/g	1.629	0.731
$b_{0,1}$	m^3/mol	-2.685 x 10^{-17}	-5.405 x 10^{-17}
$b_{0,2}$	$(m^3/mol)^2$	1.158 x 10^{-16}	1.825 x 10^{-16}
$b_{0,3}$	$(m^3/mol)^3$	5.374 x 10^{-17}	7.311 x 10^{-16}
ΔU_1	kJ/mol	-97.99	-97.99
q_{sd}	mmol/g	5.781	8.940
d_0	m^3/mol	8.773 x 10^{-12}	7.879 x 10^{-12}
ΔU_2	kJ/mol	-64.72	-64.72

4.4. Descriptions of water desorption isotherms with a hysteresis loop

The H_2O isotherm at 22°C shows a hysteresis loop between 8% RH and 22% RH (Fig. 5). As observed, the desorption loadings are higher than the adsorption loadings at the same partial pressure within the hysteresis loop. To capture this phenomenon, the desorption isotherm was treated differently. An additional term might be required to add to the adsorption isotherm model to consider the exceeding loading amounts in the hysteresis loop (Hefti et al. 2015). To avoid an isotherm model that is too complicated, the desorption isotherm is fitted separately using the same Cubic-Langmuir isotherm model. In other words, the desorption path is considered as another isotherm.

Since the experimental desorption isotherm was only measured at 22°C, the internal energy ΔU_1 and ΔU_2 were assumed to be the same as the adsorption. The total number of fitted parameters for the desorption isotherm is six parameters: q_{sb}, q_{sd}, $b_{0,1}$, $b_{0,2}$, , $b_{0,3}$, d_0, excluding ΔU_1 and ΔU_2. Using *fmincon* curve fitting tool in MATLAB (Eqn. 14), these parameters were determined and shown in Table 1. A good agreement between the fitted isotherm and the measured isotherm, as indicated in Fig. 5. At this point, we acknowledge that the isotherms here are treated as empirical expressions that could be used in process simulations and should not be used to obtain physical interpretations as they are beyond the scope of the current work.

5. H_2O dynamic column breakthrough results

5.1 Water adsorption breakthrough experiments

Water adsorption breakthrough experiments were performed at ≈22°C and 0.97 bar total pressure. At 22°C, the temperature at which the DCB studies are performed, the H_2O isotherm starts with an unfavourable (anti-Langmuir-type) behaviour followed by a favourable (Langmuir-type) behaviour. To characterize the complexity in the shape of the isotherm, three distinct positions on the H_2O adsorption isotherm were chosen, namely 8%, 22% and 45%. These values corresponded to a point below the inflection point (8% RH), a point around the inflection point (22% RH) and one point close to the H_2O saturation loading (45% RH). The detailed experimental parameters are provided in Table 3. The breakthrough curves are described in the dimensionless time $\left(\bar{t} = \frac{tv}{L}\right)$.

Table 3: List of H_2O breakthrough experiments on CALF-20

Test gas	Q_{in} [ccm]	T [°C]	P [bar]	RH [%]	$q^*_{H_2O-Ads}$ [mmol/g]	$q^*_{H_2O-Des}$ [mmol/g]
H_2O/Air	195	22.2	0.97	8.0	0.839	1.158
H_2O/Air	200	24.2	0.97	22.1	4.997	5.798
H_2O/Air	197	22.7	0.97	21.8	5.179	5.663
H_2O/Air	200	24.1	0.97	23.4	5.287	5.811
H_2O/Air	200	24.3	0.98	45.6	6.716	6.937

Various breakthrough shapes were observed as shown in Fig. 6a. A simple wave was seen at 8% RH which was below the inflection point (≈15% RH). At this RH, the isotherm has the shape of an anti-Langmuir type, which results in a simple wave transition for an adsorption breakthrough experiment (Zhang et al. 2006). For the 22% RH experiment, the breakthrough starts with a simple wave that shares a similar behaviour to the 8% RH experiment. Afterwards, a dispersed shock was observed in the H_2O breakthrough profile, which indicated a transition in the shape of the isotherm. Unlike 8% and 22% RH experiments, a very different H_2O breakthrough profile was observed in the case of 45% RH. It started with a simple wave, following by a noticeable shock until the final state was reached.

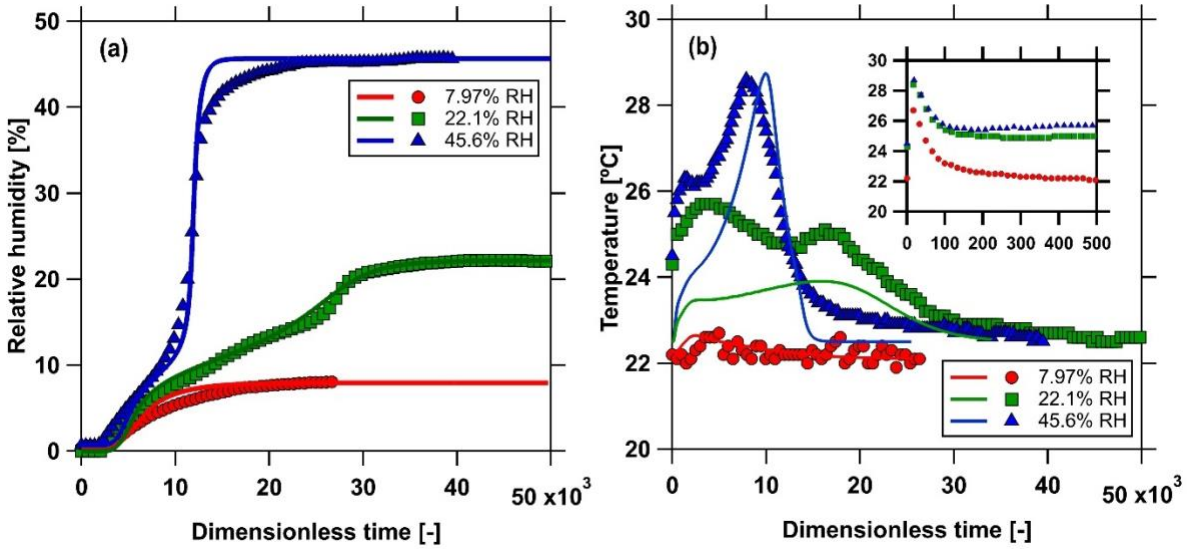

Figure 5: H_2O adsorption breakthrough curves on CALF-20 at 22°C and 0.97 bar. (a) Relative humidity curves at different RH values; (b) Temperature histories placed at 1.82 cm from the column outlet; Markers represent experimental data; Solid lines indicate simulation results. The inlay in (b) is the initial thermal breakthrough. The x axis is displayed in dimensionless time $\left(\bar{t} = \frac{tv}{L}\right)$.

Figure 7 explains the relationship between the isotherm shape and the breakthrough curve on CALF-20. The unique behaviours observed in the DCB curves could be explained based on the shape of the isotherm (Zhang et al. 2006, Mazzotti and Rajendran 2013, Rhee et al. 2014, Hefti et al. 2015). The 8% RH is located well below the inflection point (Fig. 6a), and the isotherm exhibited an unfavourable isotherm at this condition. Thus, only a simple wave was seen in the breakthrough curve at ≈8% RH. In the case of 22% RH, we observe a transition in the isotherm. The inflection point is located at ≈15% RH, and the isotherm shifts from a favourable to an unfavourable isotherm. The transitions can be represented on the isotherm using the equilibrium theory of chromatography (Rhee et al. 2014, Mazzotti and Rajendran 2013). The first transition is from 0% to ≈8% RH, the unfavourable isotherm, and the second is from 8% to the final state, i.e. 22% RH. This is translated into a simple wave and a shock front in the breakthrough curve. The 45% RH position in the isotherm is well above the inflection point. Using the same explanation, the first transition can be constructed from 0% to ≈ 8% RH and the second from 8% to 45% RH, translated into a wave and a shock front, respectively. Similar observations have been made in the

water breakthrough experiments on activated carbon, which has a type V isotherm with an inflection point (Hefti et al. 2015).

The 45% RH experiment shows that the shock elutes earlier than the 22% RH experiment (Fig. 6a). This could be explained by the H_2O adsorption isotherm at 22°C in Fig. 7a. It is well known that the shock front travels at velocity that is inversely proportional to the slope of the chord that connects the initial and final states (Rhee et al. 2014, Mazzotti and Rajendran 2013). As illustrated in Fig. 7a, the slope of the chord connecting the state corresponding to 8% RH and 45%RH is larger than that connecting the 8%RH and 22%RH. Effectively, the 22% RH and 45% RH experiments travelled through the same unfavourable region from 0% to 8% RH (Fig 7a, first line), then they showed different retention times because of the Langmuir region (Fig. 7a, second line).

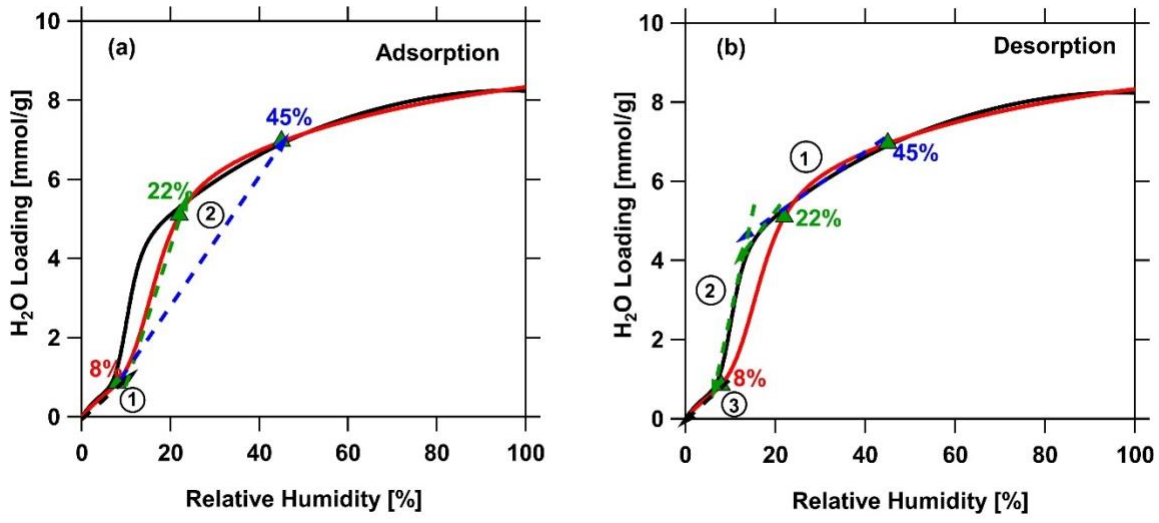

Figure 6: The H_2O adsorption (red line) and desorption (black line) isotherm on CALF-20 at 22°C. (a) The transition in the adsorption breakthrough; (b) The transition in the desorption curve

Figure 6b shows the adsorption temperature histories of the column. Overall, no significant heat wave was recorded. The 22% and 45% RH experiments recorded two separate temperature peaks. The first peak corresponded to the simple wave in the breakthrough curves. The second peak, significant in the case of 45% RH (up to ≈28.5°C), indicated the transition to a favourable isotherm behaviour in the breakthrough curves. Note that the time of these temperature peaks corresponds to the transition in the water breakthrough curves. If we look at the very beginning of each experiment, an increase of ≈4°C was seen in the temperature histories (the inlay in Fig. 6). This

can be attributed to the adsorption of nitrogen and oxygen presenting in the air, i.e., when they are not competing with water.

5.2. Water desorption breakthrough experiments

To perform the H_2O desorption experiments, the column was initially saturated with humid air at a certain RH value. Three desorption experiments at 8%, 22%, and 45% RH were examined at ≈22°C and ≈0.97 bar total pressure. Dry air was used as the purge gas in these desorption experiments. The detailed experimental parameters are provided in Table 3. The desorption curves and the column temperature histories are shown in Fig. 8.

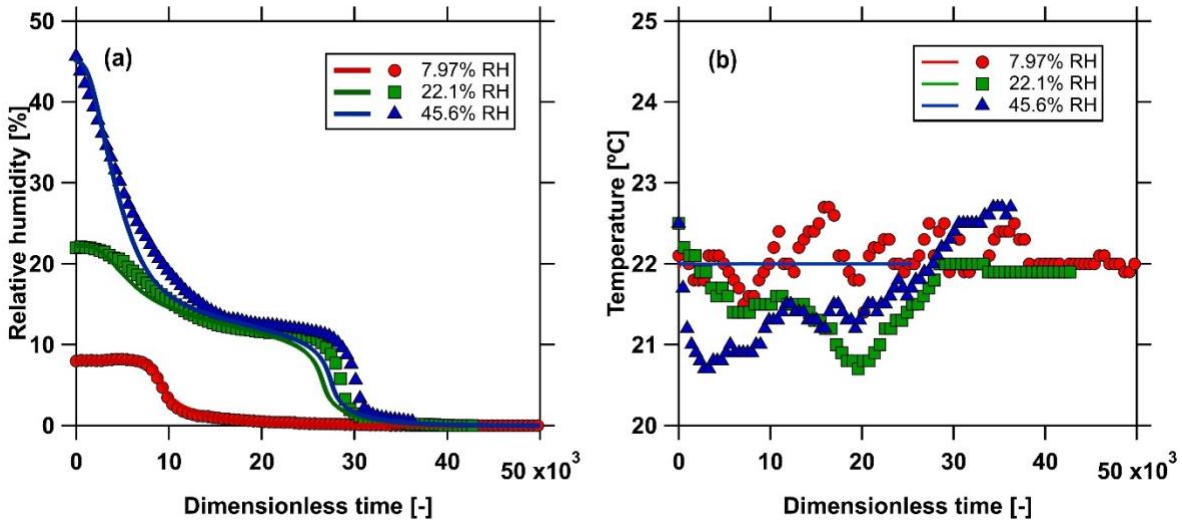

Figure 7: H_2O desorption breakthrough curves of CALF-20 at 22°C. (a) Relative humidity curves at the outlet; (b) Temperature histories at 1.82 cm from the column outlet; Markers are the experimental data; Solid lines indicate the simulation data. The x-axis is displayed in dimensionless time $\left(\bar{t} = \frac{tv}{L}\right)$.

From the H_2O desorption breakthrough curves, a shock transition was observed in the 8% RH experiment. Multiple transitions are seen for the 22% and 45% RH experiments. For both the 22% and 45% curves, the feed eluted for a while, and transition is seen until an intermediate state, characterized by a plateau, is reached. Then, a shock transition, similar to the one observed for the 8% RH, is seen. Beyond $\bar{t} \approx 15000$, the curves for 22% and 45% RH nearly overlap. It is worth noting that a $\bar{t} \approx 50000$ corresponds to multiple days of the experiment, making it challenging to

exactly reproduce the results. The time required to complete the adsorption and desorption experiments is nearly identical. This is a completely different scenario compared to the curve of favourable isotherm, where the desorption experiment takes much longer than the adsorption experiment. The attempt to reproduce the breakthrough experiments is described in Section S2 in the supporting information.

The transitions in the desorption curves can be explained based on the shape of the isotherm. In contrast with the adsorption, the desorption curve is characterized by travelling from a higher to a lower loading. The 8% RH experiment is well below the inflection point and exhibits an unfavourable isotherm. Hence, this transition results in a shock front in the desorption curve, representing this type of isotherm, which can be seen in Fig. 7b. There is no further transition in this case. Multiple transitions are observed for the 22% and 45% RH because of the inflection point at ≈15% RH. Since there is an inflection point, the isotherm could be divided into three portions corresponding to various transitions in the desorption curves. The first portion is from the initial saturation point, 22% or 45% RH, to ≈15% RH, where the inflection point is located. This part is translated into the first wave in the desorption curves (Fig. 8a). The second portion of the isotherm shows a steep change (Fig. 7b), translating into a shock front in the adsorption curve. In contrast, this transition is translated into a plateau in the desorption curve, which takes the longest time in the entire desorption experiment. The plateau is followed by a shock transition, similar to the 8% RH case, representing an unfavourable isotherm. Note that both 22% and 45% RH experiments travel the same path from 15% to 8% and from 8% to 0% (Fig. 7b). Thus, the desorption curves of 22% and 45% RH beyond $\bar{t} \approx 15000$ are nearly overlapped (Fig. 8a).

The column temperature histories from the desorption experiments are also indicated in Fig. 8b. No significant change in the temperature was seen in the desorption curves. In the 8% RH desorption experiment, the temperature fluctuated around 22°C. A decrease of ≈1.5°C was observed in the 22% and 45% RH desorption experiments. It is worth noting that the entire experiment took a couple of days to a week. Within which the laboratory temperature varies approximately ±1.0°C.

5.3. Simulating dynamic column breakthrough using the Cubic-Langmuir model

The adsorption and the desorption H_2O breakthrough curves were simulated by solving the column model described earlier. The parameters are provided in Table S2. The mass transfer between the fluid and solid phase is represented by the linear driving force (LDF) model. An LDF coefficient of k_{H2O}=0.005 s^{-1} was used for all the experiments. Three different relative humidity values were simulated and compared with the experimental curves. Both the H_2O dispersion coefficient and mass transfer coefficient are the same for the adsorption and desorption DCB simulations. The results and experimental breakthrough curves in Fig. 6 and Fig. 8 are shown.

In the adsorption breakthrough curves (Fig. 6), a good agreement between the simulations and the experiments was observed. The model captured most of the main transitions in the H_2O breakthrough profile well. The simple wave in the 8% RH experiment indicated the unfavourable part of the isotherm was well predicted. Similarly, this column model also captured the wave and the weak shock in the 22% RH. The 45% RH experiment had a small offset in the shock front. The simulation was unable to capture a slight dispersion in the shock front. This could be a limitation of the LDF model since all the resistances in the micropore and macropore were lumped as a single mass transfer coefficient *k*. Recent reports suggest that the diffusion rates change significantly with the RH values (Magnin et al., 2023, Chen et al., 2023) and variations in the spread between the simulation and experiment could be explained by accounting for these variations.

The H_2O desorption curves were also simulated and are shown in Fig. 8. In this case, the corresponding desorption isotherm was used to calculate the solid loading. The shock transition in the desorption experiment at 8% RH was predicted well. In the 22% RH and 45% RH, the H_2O desorption curves show a complicated shape with many transitions, including a semi-shock followed by a medium transition and a shock. The model captured the shapes and the transitions in the desorption profiles well. However, the simulation slightly underpredicted the retention time of the second shock in the 22% and 45% RH experiments. This can be caused by inadequate information on the hysteresis loop. It is worth noting that the hysteresis loop is located in a very narrow relative humidity range. A slight change in the RH could lead to a significant solid loading within this range. For instance, the water loadings at 13.7% and 12.0% RH are 4.15 and 3.52 mmol/g, respectively. In summary, the cubic-Langmuir model provides a relatively good description to capture the complexities involved.

The temperature histories of the column from the adsorption and desorption DCB experiments were also predicted. Fig. 6b and Fig. 8b show the predictions of the temperature curves. In the adsorption experiments, the model could capture the position of the first and second temperatures peak well. It also shows a comparable temperature magnitude. However, a difference of ≈2°C was observed in the first temperature peak. The model tends to underpredict the temperature in this case. It is worth noting that the temperature of the experiment changed only a couple of degrees, approximately 3°C - 5°C, even at 45% RH. It takes days to a week to perform an experiment, and the lab temperature slightly changed (±1°C) during the experiment. In the desorption experiments, the temperature barely changed in all experiments, and they almost overlapped. A fluctuation of ±1.5°C was observed in these experiments. On the other hand, the model shows a nearly constant temperature history for the desorption curves. In summary, the model can describe the breakthrough curves with high confidence.

5.4. Estimation of water loadings from dynamic column breakthrough experiments

All experiments were performed at ≈22°C and ≈0.97 bar total pressure. The equilibrium water loading at a specific relative humidity can be calculated for each dynamic column breakthrough experiment. The flow rate and the relative humidity at the inlet and outlet of the column were recorded for the entire experiment. The equilibrium H_2O loading for each experiment was calculated using the mass balance calculation described earlier (Eqn. 3). Table 2 provides all calculated solid loadings from the DCB experiments. The loadings measured from the DCB experiments matched well with those from the static experiments, as seen in Fig. 5. A slight difference, approximately 3%, was seen between these measurements.

6. Measurements of the competitive CO_2/H_2O isotherm

To quantify the competitive loadings of each component, the following approach consisting of two steps was used: i.) A TGA experiment with the CO_2 and H_2O mixture to measure the total loading of CO_2 + H_2O at certain RH values; and ii) A competitive adsorption breakthrough experiment to measure the competitive H_2O loading at the same RH values. The competitive CO_2 loading is then calculated from the two experiments' differences.

6.1. Total equilibrium capacity of CO_2 and H_2O

The total equilibrium loadings of CO_2 and H_2O at different relative humidity values were measured by the thermogravimetric analyzer (TGA) at ≈0.97 bar total pressure and ≈22°C. The raw experimental traces are given in Section S3 of the supporting information, and the extracted data is shown in Fig. 9. Both total loadings of the adsorption and the desorption were collected. In the adsorption experiments, the relative humidity was increased from ≈10% to 90% RH. Pure CO_2 was the carrier gas (CO_2+H_2O) to create a specific relative humidity. In the desorption experiments, the adsorbents were initially saturated with the humid CO_2 (CO_2+H_2O) at 100% RH. Then, the RH was reduced stepwise to ≈10% RH. The total weight was recorded after each step, which was the total loading of CO_2 and H_2O at a certain RH. A mass of ≈70 mg structured CALF-20 was used in these measurements. In each experiment, after around 6 hours, the change in the mass was negligible; the equilibrium was reached ($\Delta m < 0.01\%$).

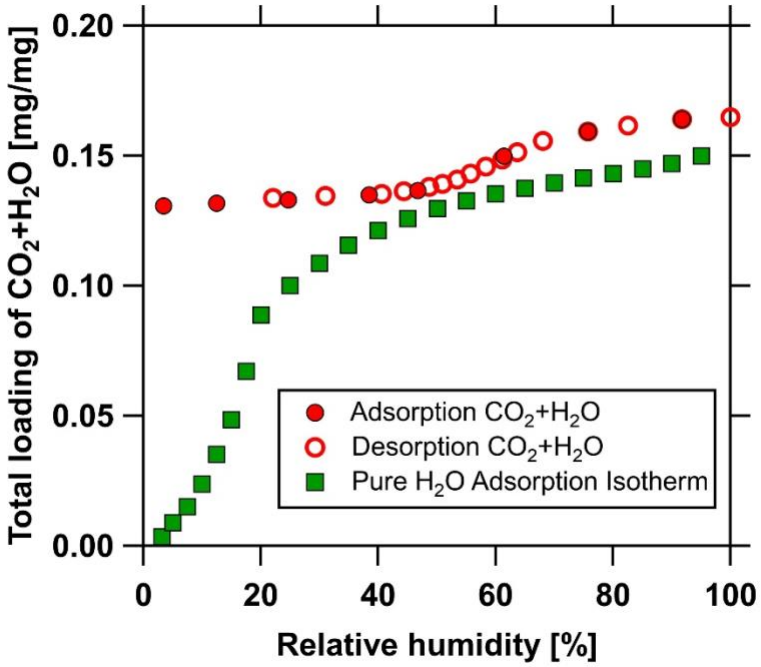

Figure 9: Total equilibrium loadings of CO_2 + H_2O at different RH values at 22°C and 0.97 bar total pressure. Filled markers indicate the adsorption data; Hollow markers represent the desorption data; Square markers are the pure H_2O adsorption isotherms for comparison.

Figure 9 shows the total equilibrium capacity of CO_2 and H_2O at 22°C and 0.97 total pressure, from 0% to 100% RH. It can be seen that the total loadings of the adsorption and the desorption are similar. This observation confirms the repeatability of the measurement, and there appears to be no hysteresis in the competitive CO_2+H_2O adsorption. The CO_2 loading at 0% RH is consistent with the pure CO_2 loadings reported earlier. At low values of RH, i.e., RH< 40%, there is a clear difference between the pure H_2O and the CO_2+H_2O experiments. Above 40% RH, the CO_2+H_2O loadings stayed slightly above the pure water loadings.

An interesting behaviour is observed in the total loadings at the RH > 60%. Higher total loading of CO_2 and H_2O is indicated (Fig. 9), which was confirmed by both adsorption and desorption measurements. The experiments at 65% and 75% RH were run for more than 48 hours to confirm the established equilibrium and that there was no artifact in the measurements. The detailed TGA measurement data is provided in the Supporting Information. There are several possibilities to explain this observation. CO_2 might strongly compete with H_2O even at high RH, and a relatively large amount of CO_2 is adsorbed. On the other hand, if we assume the water loading is similar to the pure water loading, the remaining increase in the total loading should be attributed to CO_2 adsorption. Note that at high RH, water likely fills the entire pores, leaving no site for CO_2 to be adsorbed unless there is an increase in the pore volume. This observation needs to be examined in the future.

6.2. Competitive CO_2+H_2O dynamic column breakthrough results

Traditionally, studies that dealt with CO_2+H_2O competition on strong hydrophilic adsorbents assumed that the water loading is not changed in the presence of CO_2. In the present work, we sought to relax that assumption and measure the true competitive loadings. The TGA experiments provided only the total loadings; a separate experiment was required to determine the individual contributions of CO_2 and H_2O. Accordingly, we resorted to DCB experiments. The competitive CO_2+H_2O DCB studies were performed from 13% RH to 90% RH at 22°C and 0.97 bar total pressure. A humidifier created a stable humid stream using CO_2 as the carrier gas. It takes ≈5-6 hours to create a constant humid feed. The adsorbent was activated at 150°C for 12 hours before each experiment. It is worth noting that each adsorption breakthrough needs to be run for two to three days to obtain full breakthrough curves of both H_2O and CO_2. An incomplete breakthrough will result in a false competitive loading. The CO_2 composition and the RH of the effluent were

measured by the MS and the RH meter placed at the outlet of the column. The column temperature was also recorded at 1.82 cm from the column outlet. A summary of all the CO_2+H_2O competitive DCB experiments is given in Table 4. All results are reported in dimensionless time$\left(\bar{t} = \frac{tv}{L}\right)$.

Table 4: List of CO_2+H_2O competitive adsorption DCB experiments

Test gas	Q_{in} [ccm]	T [°C]	P [bar]	RH [%]	$q^*_{H_2O}$ [mmol/g]	$q^*_{CO_2}$ [mmol/g]
CO_2/H_2O	200	22.2	0.97	13	0.137	2.95
CO_2/H_2O	200	22.5	0.97	18	0.22	2.93
CO_2/H_2O	200	24.2	0.97	23	0.45	2.90
CO_2/H_2O	200	22.7	0.97	32	1.07	2.51
CO_2/H_2O	206	23.1	0.97	47	2.08	2.00
CO_2/H_2O	200	23.1	0.97	72	7.85	0.26
CO_2/H_2O	201	22.5	0.97	87	9.01	0.03

In the competitive CO_2 breakthrough curves shown in Fig. 10 (a), the CO_2 front breaks through at $\bar{t} \approx 47$, in all experiments, and they are overlapped. The breakthrough time is also comparable with pure CO_2 adsorption breakthrough since the feed gas is rich in CO_2. Thus, the entire column is quickly filled with CO_2 in the mixture. This observation is expected since the H_2O front moves slowly through the column. Note from Fig. 10 (b) that even upto $\bar{t} \approx 100$, water has hot broken through the column. Thus, the CO_2 travels in a water-free column, which behaves similarly to the pure CO_2 breakthrough.

A new transition is observed in the CO_2 breakthrough curves when the H_2O front starts to break through the column at $\bar{t} \approx 400$. The CO_2 breakthrough curves from 13% to 47% RH show a gradual decrease in the CO_2 concentration and reach its initial concentration. However, when the relative humidity is higher than 70%, another transition is also observed in the CO_2 breakthrough curves, i.e. 73% and 87% RH. The CO_2 concentration tends to reduce faster in this second

transition. This observation could be related to the shape of the water isotherm, where an inflection point exists.

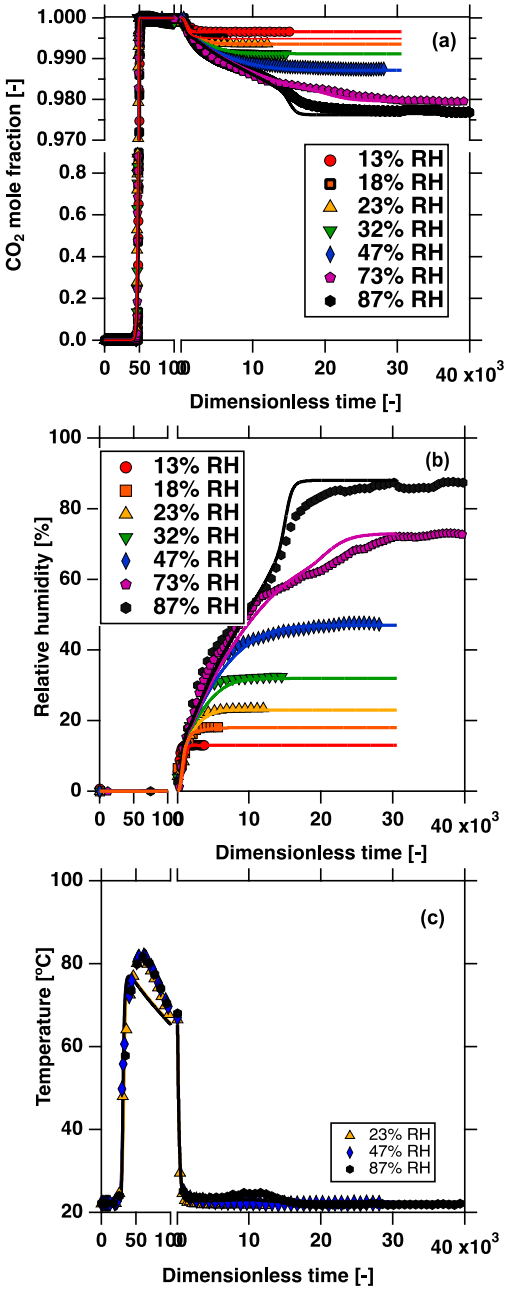

Figure 10: The competitive CO_2 breakthrough curves at various RH values at 22°C and 0.97 bar total pressure. Markers represent the experimental data. Solid lines are the simulations using the column model. (a) Competitive CO_2 breakthrough curve; (b) Competitive H_2O breakthrough curves; (c) Column temperature history at 1.82 cm from the column outlet.

Figure 10 (b) shows the competitive H_2O breakthrough curves at various RH values and the corresponding temperature histories of the CO_2+H_2O breakthrough experiments. Note that since CO_2 has already broken through the column, the H_2O front travels in an environment of CO_2. A simple wave is observed in the breakthrough curves from 13% to 47% RH experiments. Furthermore, a second transition in the H_2O breakthrough curves is also seen at 73% and 87% RH. This observation suggests that the competitive H_2O isotherm also contains an inflection point, which results in different behaviours of the breakthrough curves depending on the relative humidity. This transition in the H_2O breakthrough curves also confirms why the CO_2 breakthrough curves at these two RH values were distinctly different.

The temperature histories show a peak at $\bar{t} \approx 40$), corresponding to the heat generated by the CO_2 adsorption. The temperature quickly increases and reaches ≈80°C (Fig. 10c), after which the temperature starts to drop, except a small bump at $\bar{t} \approx 10000$ at 87% RH. This small change in the temperature is caused by the H_2O adsorption at high relative humidity, where the transition in the H_2O breakthrough curves occurs. This observation suggests that a non-negligible amount of water is adsorbed, resulting in a higher temperature.

Figure 11 compares the single and competitive H_2O breakthrough curves at 13% and 47% RH. The square markers represent the single-component H_2O breakthrough experiments using instrument air as the carrier gas. The circle markers indicate the competitive H_2O breakthrough profiles using CO_2 as the carrier gas. At 13% RH, the H_2O broke through very early in the binary CO_2+H_2O breakthrough experiment, at $\bar{t} \approx 300$. In contrast, it took $\bar{t} \approx 5000$ for water to break through in the pure H_2O experiment at the same RH. Similarly, at 47% RH, the competitive H_2O experiment broke through earlier than the single H_2O experiment. This observation suggests that water adsorption is strongly affected by the presence of CO_2 at low to intermediate RH. The area behind the breakthrough curves is considered as the accumulated water loading. It is seen that the area behind the competitive water breakthrough curve is significantly reduced compared to the pure water breakthrough curve. Thus, much lower water loading would be expected in the presence of CO_2. It must be re-emphasized that CALF-20 is a physisorbent CO_2 capture material, and the difference in boiling point of CO_2 and water is 178 °C. In that light, the impact of CO_2 on H_2O is indeed intriguing. Recently, Ho and Paesani used molecular dynamics to explain the competitive behaviour of H_2O and CO_2 on CALF-20 (Ho and Paesani, 2023). They showed that ton he presence

of CO_2, water molecules form a more connected hydrogen-bonded network which decreases water entropy leading to a retardation in its capacity. Such a unique behaviour where the presence of CO2 retards H_2O adsorption, to the best of our knowledge, has not been noticed before.

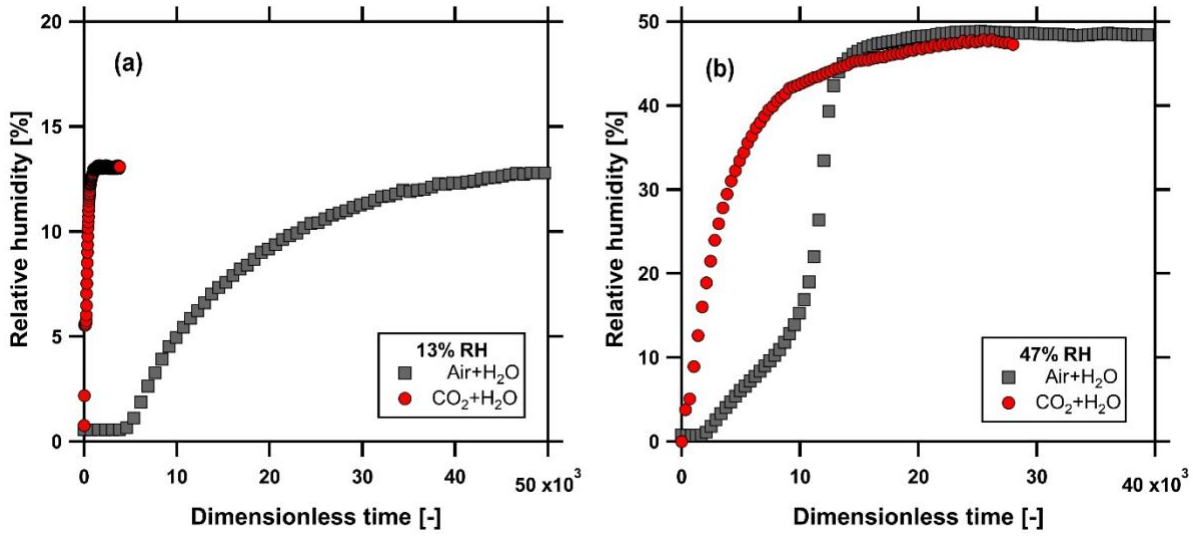

Figure 11: A comparison of single and competitive H_2O breakthrough curves. (a) 13% RH and (b) 47% RH. Squares indicate the single H_2O breakthrough curves using air as the carrier gas; Circles show the competitive H_2O breakthrough curves using CO_2 as the carrier gas. The experiments were performed at ≈22°C and 0.97 bar total pressure.

Furthermore, comparing the shape of the breakthrough curves is also insightful. A simple wave is observed in the binary CO_2+H_2O breakthrough curve at 47% RH, instead of a wave followed by a shock front in the single-component H_2O breakthrough experiment (Fig. 11b). Note that the pure water isotherm contains an inflection point at ≈15% RH (Fig. 7). Hence, a transition in the pure water breakthrough curve is seen beyond 15% RH. It nearly reaches the saturation loading at 47% RH. The competitive CO_2+H_2O breakthrough at 47% RH, on the other hand, shows a completely different behaviour. The water breakthrough curve in this case only shows a simple wave. The breakthrough time is much shorter (Fig. 11b). This observation implies that in the presence of CO2, at 47%RH, the water isotherm is still unfavourable. In contrast, in the case of the pure water isotherm, we are towards the right of the inflection point at this RH. Under the presence of CO_2, the H_2O tends to break through significantly earlier, which suggests a dramatic reduction of the H_2O loadings. This observation contrasts sharply with zeolite 13X, where there is no difference in

the single and binary water breakthrough profiles. In other words, CO2 does not affect H_2O adsorption in zeolite 13X (Wilkins et al. 2020).

At high relative humidity (RH>70%), the competitive H_2O breakthrough curves show a transition in their breakthrough curves (Fig. 10a). This means an inflection point still exists in the competitive H_2O isotherm, and it changes from an unfavourable to a favourable type of isotherm. Beyond the inflection point, the adsorption of H_2O becomes significant, hindering the CO_2 adsorption. The result from the pure H_2O breakthrough study showed the transition in the water breakthrough curve at 22% RH. This transition is not observed in the competitive CO_2+H_2O breakthrough until the relative humidity exceeds 70% RH. Thus, the inflection point in the competitive H_2O isotherm must be shifted to higher relative humidity.

6.3. Estimation of the competitive CO_2+H_2O isotherm

To estimate the competitive loading of H_2O, the competitive water loadings were calculated by performing a mass balance around the column using the Eqn. (3). The total loadings of CO_2 and H_2O at similar relative humidity were also measured by thermogravimetry analysis. The competitive CO_2 loadings were obtained by the difference between the total and competitive water loading at various relative humidity. Using Eqn. 4, the CO_2 capacity can also be estimated directly from the DCB experiments. (4), but it is challenging in a binary system where the heavy component is strongly adsorbed, and the uncertainties build up in a long experiment, i.e. up to three days.

Figure 12 shows the competitive isotherms of CO_2 and H_2O at 22°C and 0.97 total pressure. An interesting observation is seen in the competitive CO_2 loading. At low relative humidity (RH<20%), the CO_2 capacity barely changes, while only a small amount of H_2O adsorbed. This observation is consistent with the previous competitive breakthrough curves. The binary water breakthrough curve at 13% (Fig. 11a) also confirmed a significant loss of H_2O capacity in the presence of CO_2. These results demonstrate that water does not affect the adsorption of CO_2 when the relative humidity is smaller than 20%. From 20% to 40% RH, the CO_2 capacity slightly decreases. It is worth noting that the competitive CO_2 loading on CALF-20 is still relatively high (>2.00 mol/g) at low to intermediate relative humidity (RH<40%). From 50% to 70% RH, the CO_2 capacity drops as water adsorption strengthens. When the RH is beyond 70%, the competitive CO_2 loading is very small.

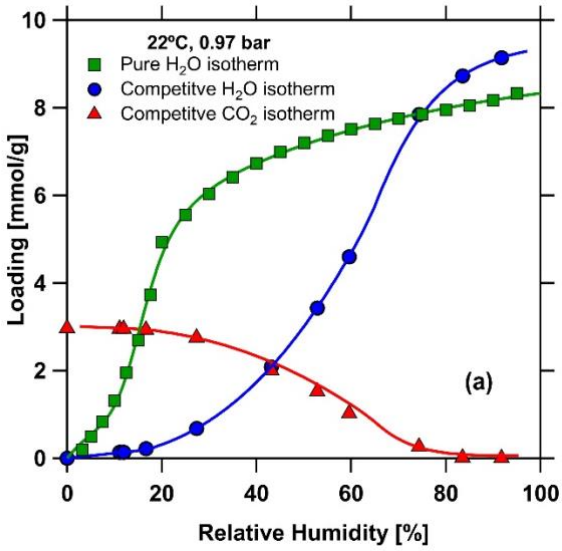

Figure 12: Competitive CO_2+H_2O equilibrium loadings on CALF-20 at 22°C and 0.97 bar collected from TGA and DCB experiments. (a) The competitive loading of CO_2 and H_2O at various relative humidity. Markers are the experimental data from binary dynamic column breakthrough experiments and thermogravimetry analysis. Solid lines are used to guide the eye.

A type V isotherm with an inflection point is still observed in the competitive H_2O isotherm. The pure H_2O isotherm, at 22°C and 0.97 bar, the inflection point is located at ≈15% RH. In the binary CO_2+H_2O isotherm, the inflection point shifts further to the high relative humidity at ≈65%. This unique transition is reflected in the shape of the breakthrough curves. For instance, the binary CO_2+H_2O breakthrough at 47% RH (Fig. 12b) only shows a wave instead of a wave and a shock front in the pure H_2O breakthrough. This result reinforces that water has not passed the inflection point yet and still exhibits an unfavourable isotherm, resulting in a simple wave in the breakthrough curve. At high RH, a wave and a shock front were observed in the binary CO_2+H_2O breakthrough, i.e., at 73% RH and 87% RH (Fig. 11a). At this point, water has travelled through the inflection point, and it exhibits a favourable isotherm, where water is strongly adsorbed.

7. Modelling the competition of CO_2 and H_2O

7.1. Description of the competitive CO_2/H_2O isotherm

Due to a complex, competitive adsorption behaviour, an empirical model was developed to describe the binary CO_2+H_2O adsorption. Hefti and Mazzotti introduced a modified Sips model to describe the competition of CO_2 and H_2O on zeolite 13X (Hefti et al. 2018). Wilkins *et al*. proposed

a modification to the Langmuir model to account for the impact of water on the CO_2 loadings on zeolite 13X (Wilkins et al. 2020). A similar approach was used in this study to express the competitive CO_2 loadings on CALF-20. The pure CO_2 isotherm expression was adjusted to reflect the impact of water. Three more parameters, λ_1, λ_2 and λ_3, were added to describe a reduction of the CO_2 loadings in the presence of water:

$$q^*_{CO_2} = \frac{1}{1+\lambda_1 {q^*_{H_2O}}^{\lambda_3}}\left[\frac{q_{sb,CO_2} b_{CO_2} C_{CO_2}}{(1+b_{CO_2} C_{CO_2})}\right] + \frac{1}{1+\lambda_2 {q^*_{H_2O}}^{\lambda_3}}\left[\frac{q_{sd,CO_2} d_{CO_2} C_{CO_2}}{(1+d_{CO_2} C_{CO_2})}\right] \quad (19)$$

In the above isotherm function, the pure component parameters $b_{CO_2}, bd_{CO_2}, q_{sb,CO_2}, q_{sd,CO_2}$ are pure component parameters reported by Nguyen et al. (Nguyen et al., 2022) and provided in Section S4 of the supporting information. As can be seen for the pure CO_2 case, i.e., in the absence of water, the above isotherm will retain all the features of the dual-site isotherm presented in our previous study. In this modified isotherm, although the CO_2 loading is described as a function of the water loading, temperature and the concentration of CO_2, we hasten to add that the temperature and CO_2 concentration dependence is unlikely to be descriptive and should be used cautiously. Establishing the complete dependence will require additional experiments where a full matrix of CO_2 concentration, RH and temperatures are explored. We note that the above competitive isotherm may be reasonable to simulate the experiments performed in this study. By fitting the above parameters to the competitive CO2 loadings, we obtain the values of l to be λ_1=0.0066, λ_2=2.483 and λ_3=3.55.

The impact of CO_2 on H_2O is rather unusual. Recent works have sought to explain this behaviour. Without the availability of further data, we decided not to describe the competitive H_2O isotherm. Instead, we used the idea of discrete equilibrium data where the isotherm is described directly using the experimentally determined one using a piecewise linear interpolation function (Rajendran et al., 2020, Haghpanah et al., 2012). In the adsorption experiments, since there is a considerable difference in the breakthrough times of CO_2 and H_2O, it is reasonable to assume that H_2O always travels in a background of CO_2. Hence, the competitive H_2O isotherm is sufficient to describe the breakthrough dynamics

7.2. Binary CO_2/H_2O dynamic column breakthrough simulations

The competitive CO_2+H_2O breakthrough curves at various relative humidity can be predicted by solving the detailed model described earlier. The bed is split into 30 cells, and the finite volume method with a total variation diminishing (TVD) scheme is used to discretize all equations (Haghpanah et al. 2013). The resulting ordinary differential equations (ODE) are solved by *ode23s* using MATLAB ODE solver. The specific solution methodology can be found in the previous study (Haghpanah et al. 2013). The simulated results are compared with the experimental breakthrough curves and shown in Fig. 4 and Fig. 5. Both breakthrough curves and the temperature history of the column are reported.

The competitive CO_2 concentration curves (Fig. 10) show a good agreement between the simulations and the experiments. The model captures the CO_2 breakthrough time well and can predict the "roll-up" effect when H_2O breaks through the column. The second transition in the CO_2 breakthrough curves at 73% and 87% RH is also predicted well. The competitive CO_2 loadings need to be predicted properly with and without water. Initially, the CO_2 travels through the column without H_2O since the feed gas is rich in CO_2, and H_2O slowly moves across the column. In this case, the CO_2 loadings are similar to the pure CO_2 isotherms. Afterwards, the water builds up in the adsorbents, and there is competitive adsorption between CO_2 and H_2O. As a result, the CO_2 loading reduces with increasing relative humidity. Another important note is that the adsorption of CO_2 releases a significant amount of heat in the column. At higher temperatures, the CO_2 loadings will be lower. Without considering the effect of temperature, the CO_2 breakthrough time will be overpredicted. The modified Langmuir model considers both the effect of water loading and the temperature on the CO_2 adsorption. Thus, all experiments show a good agreement between the simulation and the experiments, from 13% to 87% RH.

The discrete equilibrium model also predicts the competitive H_2O breakthrough curves at different relative humidity well (Fig. 11a). A simple wave is indicated in the dynamic column breakthrough simulations at the RH < 47%. The transition in the competitive H_2O breakthrough curves is also captured at 73% and 87%. The wave and the shock front in the water curves are predicted, indicating the inflection point in the isotherm.

Figure 11b shows the temperature history of the column at 1.82 cm from the column outlet. A temperature peak at $\bar{t} \approx 40$ is recorded with a maximum value of ≈80°C. The model can predict the

temperature's position and magnitude in all experiments. The decay in the temperature after reaching its peak is also well captured. Afterward, the temperature fluctuates in a small range of temperatures, approximately ≈22°C. Briefly, the column model adequately simulates the competitive CO_2+H_2O breakthrough on CALF-20 in a wide relative humidity range. Both the breakthrough curves and temperature history are predicted. The modified Langmuir isotherm model is suitable to describe the competitive CO_2 loading as a function of water loading and temperature. The discrete equilibrium data is also sufficient to describe the competitive water loading in all CO_2+H_2O breakthrough experiments.

8. Conclusions

Adsorption equilibria of water on CALF-20 MOF were measured by thermogravimetric analyzer from 0 bar to 0.027 bar partial pressure at 22, 30, 40, 50, 60, 80 and 100°C. A volumetric apparatus was also used to measure the H_2O isotherm from 0 bar to 0.027 bar partial pressure at 22°C. The H_2O isotherms showed an inflection point, indicating a transition in the shape of the isotherm. At low relative humidity values, the adsorbed amount of H_2O is very small (<0.5 mmol/g), which means CALF-20 exhibits an unfavourable isotherm under these conditions. The cubic-Langmuir model was applied to describe the pure H_2O isotherms.

The adsorption and the desorption breakthrough experiments were performed at 22°C and 0.97 bar total pressure. Three different relative humidity values were chosen: 8%, 22% and 45%, which translates to a point under the inflection point, around the inflection point, and beyond that. The breakthrough curves show many transitions and shapes depending on the feed's relative humidity. These unique breakthrough curves reflect complexity in the shape of the isotherm. The equilibrium loadings of water collected from DCB experiments were comparable (within 3%) to the volumetric and thermogravimetric measurements.

This study shows that the competitive CO_2 and H_2O loadings over a range of relative humidities can be estimated by combining the thermogravimetric analysis (TGA) and the binary dynamic column breakthrough (DCB) measurement. CALF-20 shows unique competitive adsorption between CO_2 and H_2O. At the RH < 20%, the competitive CO_2 loadings are comparable to pure CO_2 loading. This result indicates that, despite CALF-20 being a physisorbent, water does not strongly affect CO_2 . Using an empirical expression, the model described the competitive breakthrough curves well.

The success of a CO_2 capture sorbent rests, among many other features, on its ability to work in the presence of H_2O. Hence, measuring H_2O, and competitive CO_2+H_2O isotherms is critical. These measurements, the competitive ones in particular, are time-consuming and perhaps not performed for materials at an early stage of development. In this manuscript, we demonstrate that such data can be measured using instruments considered readily accessible. While these measurements are indeed time-consuming, their value cannot be overstated. The data is vital not

only for process design but also to support efforts in molecular simulations. Water continues to be one of the more challenging systems to describe. The available data such as the one described can help calibrate force fields and make these tools available for screening databases. The measurements also help reveal new phenomena, e.g. suppression of H_2O by CO_2 on a physisorbent, which might be observed in other systems, provided the correct experiments are performed. These measurements will help us unlock adsorption phenomena and possibly design new capture materials.

NOMENCLATURE

c	Concentration [mol m^{-3}]
b_1	Isotherm constant [mol^{-1} m^3]
b_2	Isotherm constant [mol^{-2} m^6]
b_3	Isotherm constant [mol^{-3} m^9]
$C_{p,g}$	Specific heat of gas [J mol^{-1} K^{-1}]
$C_{p,w}$	Specific heat of column wall [J mol^{-1} K^{-1}]
$C_{p,a}$	Specific heat of adsorbed phase [J mol^{-1} K^{-1}]
d	Isotherm constant [mol^{-1} m^3]
ΔH	Enthalpy of adsorption [J mol^{-1}]
D_L	Axial dispersion [m^2 s]
D_m	Molecular diffusion coefficient [m^2 s]
D_p	Pore diffusion coefficient [m^2 s]
h_{in}	Inside heat transfer coefficient [W m^{-2} K^{-1}]
h_{out}	Outside heat transfer coefficient [W m^{-2} K^{-1}]
J	Objective function [-]
k	LDF coefficient [s^{-1}]
K_z	Effective gas thermal conductivity [J m^{-2} K^{-2} s^{-1}]
L	Column length [m]
m_{ads}	Mass of adsorbent [kg]
n	Moles [mol]
P	Pressure [Pa]
q	Solid phase loading [mol m^{-3}]
Q	Volumetric flow rate [m^3 s^{-1}]
Q^*	Equilibrium solid loading [mol kg^{-1}]
q_s	Saturation capacity [mol kg^{-1}]
R	Universal gas constant [Pa m^3 mol^{-1} K^{-1}]
r_{in}	Inside radius of column [m]
r_{out}	Outside radius of column [m]
r_p	Particle radius [m]
T	Time [s]
T	Temperature [K]
T_w	Wall temperature [K]

T_{amb}	Ambient temperature [K]
v	Velocity [m s^{-1}]
y	Gas phase composition [-]
z	Axial distance [m]

Greek Symbols

ε	Bed voidage [-]
μ	Fluid viscosity [kg m^{-1} s^{-1}]
ρ_p	Adsorbent particle density [kg m^{-3}]
ρ_w	Column wall density [kg m^{-3}]
τ	Tortuosity [-]

Abbreviations

RH	Relative Humidty

ACKNOWLEDGEMENTS

We acknowledge funding from Alberta Innovates Strategic development grant, Natural Sciences and Engineering Research Council (NSERC) of Canada through the CREATE Grant.

SUPPORTING INFORMATION

Supporting information contains description of H_2O isotherms as a function of RH; reproducibility of breakthrough experiments; Experimental thermogravimetric analysis traces of various experiments pure CO_2 isotherm parameters; Breakthrough simulation parameters; Table with pure H_2O equilibrium loading at various temperatures.

AUTHOR CONTRIBUTIONS

Tai T.T. Nguyen: Conceptualization, Methodology, Experimentation, Formal Analysis, Writing-Original Draft, Writing- Review and Editing; **B. M. Balasubramaniam**: Experimentation,

Formal Analysis, Review and Editing; **N. Fylstra**: Experimentation, Formal Analysis, Review and Editing; **R. P.S. Hyunh**: Experimentation, Formal Analysis, Review and Editing; **A. Rajendran**: Conceptualization, Methodology, Writing- Review and Editing, Supervision, Funding acquisition; **G. KH Shimizu**: Writing- Review and Editing, Supervision, Funding acquisition.

DECLARATION OF INTERESTS

Two patents (CA2904546A1 and EP3784824A1) related to CALF-20 are licensed for different fields of use. GKHS receives royalties from the license. TTTN and RPSH are employed by Svante Inc which has commercialized CALF-20 for Industrial CO_2 capture. The other authors do not have any competing interests

BIBLIOGRAPHY

Altintas, C., G. Avci, H. Daglar, A. Nemati Vesali Azar, S. Velioglu, I. Erucar and S. Keskin (2018). "Database for CO_2 separation performances of MOFs based on computational materials screening." *ACS Appl Mater Inter* **10**(20): 17257-17268.

Bahamon, D., A. Díaz-Márquez, P. Gamallo and L. F. Vega (2018). "Energetic evaluation of swing adsorption processes for CO_2 capture in selected MOFs and zeolites: Effect of impurities." *Chem Eng J* **342**: 458-473.

Baker, G. A., G. A. Baker Jr, G. Baker, P. Graves-Morris and S. S. Baker (1996). Pade Approximants: Encyclopedia of Mathematics and It's Applications, Vol. 59 George A. Baker, Jr., Peter Graves-Morris, Cambridge University Press.

Belmabkhout, Y., R. Serna-Guerrero and A. Sayari (2010). "Amine-bearing mesoporous silica for CO_2 removal from dry and humid air." *Chem Eng Sci* **65**(11): 3695-3698.

Ben-Mansour, R., N. A. Qasem and M. A. Antar (2018). "Carbon dioxide adsorption separation from dry and humid CO_2/N_2 mixture." *Comp Chem Eng* **117**: 221-235.

Burtch, N. C., H. Jasuja and K. S. Walton (2014). "Water stability and adsorption in metal–organic frameworks." *Chem Rev* **114**(20): 10575-10612.

Canivet, J., A. Fateeva, Y. Guo, B. Coasne and D. Farrusseng (2014). "Water adsorption in MOFs: fundamentals and applications." *Chem Soc Rev* **43**(16): 5594-5617.

Chanut, N., S. Bourrelly, B. Kuchta, C. Serre, J. S. Chang, P. A. Wright and P. L. Llewellyn (2017). "Screening the effect of water vapour on gas adsorption performance: application to CO_2 capture from flue gas in metal–organic frameworks." *ChemSusChem* **10**(7): 1543-1553.

Chen, Z., C-H. Ho, X. Wang, S.M. Vornholt, T. M. Rayder, T. Islamoglu, O.K. Farha, F. Paesani and K.W. Chapman (2023). " Humidity-Responsive Polymorphism in CALF-20: A Resilient MOF Physisorbent for CO2 Capture" *ACS Mater Lett.*, In Press

Choi, S., M. L. Gray and C. W. Jones (2011). "Amine‐tethered solid adsorbents coupling high adsorption capacity and regenerability for CO_2 capture from ambient air." *ChemSusChem* **4**(5): 628-635.

Dureckova, H. (2018). Robust Machine Learning QSPR Models for Recognizing High Performing MOFs for Pre-Combustion Carbon Capture and Using Molecular Simulation to Study Adsorption of Water and Gases in Novel MOFs, MSc Thesis, Université d'Ottawa/University of Ottawa.

Gebald, C., J. A. Wurzbacher, A. Borgschulte, T. Zimmermann and A. Steinfeld (2014). "Single-component and binary CO_2 and H_2O adsorption of amine-functionalized cellulose." *Env Sci Tech* **48**(4): 2497-2504.

Gebald, C., J. A. Wurzbacher, P. Tingaut, T. Zimmermann and A. Steinfeld (2011). "Amine-based nanofibrillated cellulose as adsorbent for CO_2 capture from air." *Env Sci Tech* **45**(20): 9101-9108.

Gelles, T., S. Lawson, A. A. Rownaghi and F. Rezaei (2020). "Recent advances in development of amine functionalized adsorbents for CO_2 capture." *Adsorption* **26**(1): 5-50.

Goyal, P., M. J. Purdue and S. Farooq (2020). "Adsorption and diffusion of moisture and wet flue gas on silica gel." *Chem Eng Sci* **227**: 115890.

Haghpanah, R., A. Rajendran, S. Farooq I.A. Karimi and M. Amanullah. " Discrete equilibrium data from dynamic column breakthrough experiments ." *Ind Eng Chem Res* **51**(45): 14834-14844.

Haghpanah, R., A. Majumder, R. Nilam, A. Rajendran, S. Farooq, I. A. Karimi and M. Amanullah (2013). "Multiobjective optimization of a four-step adsorption process for postcombustion CO_2 capture via finite volume simulation." *Ind Engg Chem Res* **52**(11): 4249-4265.

Hefti, M., L. Joss, D. Marx and M. Mazzotti (2015). "An experimental and modeling study of the adsorption equilibrium and dynamics of water vapor on activated carbon." *Ind Engg Chem Res* **54**(48): 12165-12176.

Hefti, M. and M. Mazzotti (2018). "Postcombustion CO_2 capture from wet flue gas by temperature swing adsorption." *Ind Engg Chem Res* **57**(45): 15542-15555.

Hill, T. (1960). "An Introduction to Statistical Thermodynamics, Adison-Wesley." Reading, MA.

Ho, C-H and F. Paesani (2023). "Ho, C. H., & Paesani, F. (2023). "Elucidating the Competitive Adsorption of H_2O and CO_2 in CALF-20: New Insights for Enhanced Carbon Capture Metal–Organic Frameworks". *ACS App Mater Inter* In Press.

Ilić, M., D. Flockerzi and A. Seidel-Morgenstern (2010). "A thermodynamically consistent explicit competitive adsorption isotherm model based on second-order single component behaviour." *J Chromatogr A* **1217**(14): 2132-2137.

Kizzie, A. C., A. G. Wong-Foy and A. J. Matzger (2011). "Effect of humidity on the performance of microporous coordination polymers as adsorbents for CO_2 capture." *Langmuir* **27**(10): 6368-6373.

Li, G., P. Xiao, P. A. Webley, J. Zhang and R. Singh (2009). "Competition of CO_2/H_2O in adsorption based CO_2 capture." *Energy Procedia* **1**(1): 1123-1130.

Lin, J.-B., T. T. Nguyen, R. Vaidhyanathan, J. Burner, J. M. Taylor, H. Durekova, F. Akhtar, R. K. Mah, O. Ghaffari-Nik, S. Marx, N. Fylstra, S. S. Iremonger, K. W. Dawson, P. Sarkar, P. Hovington, A. Rajendran, T. K. Woo and G. K. Shimizu (2021). "A scalable metal-organic framework as a durable physisorbent for carbon dioxide capture." *Science* **374**(6574): 1464-1469.

Liu, J., Y. Wang, A. I. Benin, P. Jakubczak, R. R. Willis and M. D. LeVan (2010). "CO_2/H_2O adsorption equilibrium and rates on metal– organic frameworks: HKUST-1 and Ni/DOBDC." *Langmuir* **26**(17): 14301-14307.

Liu., J., Y. Wang., A. I. Benin., P. Jakubczak., R. R. Willis. and M. D. LeVan. (2010). "CO_2/H_2O Adsorption Equilibrium and Rates on Metal-Organic Frameworks: HKUST-1 and Ni/DOBDC." *Langmuir* **26**: 14301.

Lorek, A. and J. Majewski (2018). "Humidity Measurement in Carbon Dioxide with Capacitive Humidity Sensors at Low Temperature and Pressure." *Sensors* **18**(8): 2615.

Magnin, Y., D. Estelle, G. Maurin, P. Llewellyn (2023). "Abnormal CO_2 and H_2O diffusion in CALF-20 (Zn) Metal-Organic Angstropores"., arXiv prepring 2307.09200

Martinez, G. M. and D. Basmadjian (1996). "Towards a general gas adsorption isotherm." *Chem Eng Sci* **51**(7): 1043-1054.

Mazzotti, M. and A. Rajendran (2013). "Equilibrium theory–based analysis of nonlinear waves in separation processes." *Annu Rev Chem Biomol 4*: 119-141.

Myers, A. L. and J. M. Prausnitz (1965). "Thermodynamics of mixed‐gas adsorption." *AIChE J* **11**(1): 121-127.

Nguyen, T. T. (2021). Humid Post-Combustion CO2 Capture By Vacuum Swing Adsorption Using CALF-20, PhD Thesis, University of Alberta.

Nguyen, T. T., J.-B. Lin, G. K. Shimizu and A. Rajendran (2022). "Separation of CO_2 and N_2 on a hydrophobic metal organic framework CALF-20." *Chem Eng J* **442**: 136263.

Nguyen, T. T. T., G. K. Shimizu and A. Rajendran (2022). "CO_2/N_2 separation by vacuum swing adsorption using a metal-organic framework, CALF-20: Multi-objective optimization and experimental validation." *Chem Eng J:* 139550.

Pai, K. N., J. D. Baboolal, D. A. Sharp and A. Rajendran (2019). "Evaluation of diamine-appended metal-organic frameworks for post-combustion CO_2 capture by vacuum swing adsorption." *Sep Purif Technol* **211**: 540-550.

Pirngruber, G. D., L. Hamon, S. Bourrelly, P. L. Llewellyn, E. Lenoir, V. Guillerm, C. Serre and T. Devic (2012). "A method for screening the potential of MOFs as CO_2 adsorbents in pressure swing adsorption processes." *ChemSusChem* **5**(4): 762-776.

Qasem, N. A. and R. Ben-Mansour (2018). "Adsorption breakthrough and cycling stability of carbon dioxide separation from $CO_2/N_2/H_2O$ mixture under ambient conditions using 13X and Mg-MOF-74." *Applied Energy* **230**: 1093-1107.

Rajagopalan, A. K., A. M. Avila and A. Rajendran (2016). "Do adsorbent screening metrics predict process performance? A process optimisation based study for post-combustion capture of CO_2." *Int J Greenh Gas Con* **46**: 76-85.

Rajendran, A., R. Maruyama, H.O.R. Landa and A. Seidel-Morgenstern (2020)." binar Modellingy non-linear chromatoraphy using discrete equilibrium data" *Adsorption* **26**: 973-987.

Rajendran, A., G. K-H. Shimizu and T.K. Woo (2023)."The Challenge of Water Competition in Physical Adsorption of CO2 by Porous Solids for Carbon Capture Applications–A Short Perspective. " *Adv Mater* 2301730

Rhee, H.-K., R. Aris and N. R. Amundson (2014). First-order partial differential equations, Courier Corporation.

Ruthven, D. M. (1984). Principles of adsorption and adsorption processes, John Wiley & Sons.

Silva, M., A. Ribeiro, C. Silva, I. Nogueira, K.-H. Cho, U.-H. Lee, J. Faria, J. Loureiro, J.-S. Chang and A. Rodrigues (2021). "MIL-160 (Al) MOF's potential in adsorptive water harvesting." *Adsorption* **27**(2): 213-226.

Stampi-Bombelli, V., M. van der Spek and M. Mazzotti (2020). "Analysis of direct capture of CO_2 from ambient air via steam-assisted temperature–vacuum swing adsorption." *Adsorption* **26**(7): 1183-1197.

Sumida, K., D. L. Rogow, J. A. Mason, T. M. McDonald, E. D. Bloch, Z. R. Herm, T.-H. Bae and J. R. Long (2012). "Carbon dioxide capture in metal–organic frameworks." *Chem Rev* **112**(2): 724-781.

Thommes, M. (2010). "Physical adsorption characterization of nanoporous materials." *Chem Ing Tech* **82**(7): 1059-1073.

Thommes, M., K. Kaneko, A. V. Neimark, J. P. Olivier, F. Rodriguez-Reinoso, J. Rouquerol and K. S. Sing (2015). "Physisorption of gases, with special reference to the evaluation of surface area and pore size distribution (IUPAC Technical Report)." *Pur Appl Chem* **87**(9-10): 1051-1069.

Thommes, M., B. Smarsly, M. Groenewolt, P. I. Ravikovitch and A. V. Neimark (2006). "Adsorption hysteresis of nitrogen and argon in pore networks and characterization of novel micro-and mesoporous silicas." *Langmuir* **22**(2): 756-764.

Varghese, A. M. and G. N. Karanikolos (2020). "CO_2 capture adsorbents functionalized by amine–bearing polymers: A review." *Int J Greenh Gas Con* **96**: 103005.

Velasco, L. F., R. Guillet-Nicolas, G. Dobos, M. Thommes and P. Lodewyckx (2016). "Towards a better understanding of water adsorption hysteresis in activated carbons by scanning isotherms." *Carbon* **96**: 753-758.

Wilkins, N. S. and A. Rajendran (2019). "Measurement of competitive CO_2 and N_2 adsorption on Zeolite 13X for post-combustion CO_2 capture." *Adsorption* **25**(2): 115-133.

Wilkins, N. S., J. A. Sawada and A. Rajendran (2020). "Measurement of competitive CO_2 and H_2O adsorption on zeolite 13X for post-combustion CO_2 capture." *Adsorption*.

Xiao, P., J. Zhang, P. Webley, G. Li, R. Singh and R. Todd (2008). "Capture of CO_2 from flue gas streams with zeolite 13X by vacuum-pressure swing adsorption." *Adsorption* **14**(4-5): 575-582.

Yaghi, O. M., H. Li, M. Eddaoudi and M. O'Keeffe (1999). "Design and synthesis of an exceptionally stable and highly porous metal-organic frameworks." *Nature* **42**: 276-279.

Yu, J., L.-H. Xie, J.-R. Li, Y. Ma, J. M. Seminario and P. B. Balbuena (2017). "CO_2 capture and separations using MOFs: computational and experimental studies." *Chem Rev* **117**(14): 9674-9754.

Zhang, W., Y. Shan and A. Seidel-Morgenstern (2006). "Breakthrough curves and elution profiles of single solutes in case of adsorption isotherms with two inflection points." *J Chromatogr A* **1107**(1-2): 216-225.